Geochemistry, Geophysics, Geosystems

RESEARCH ARTICLE
10.1029/2021GC009686

Key Points:

- Late Cenozoic lavas are predominantly derived from a peridotitic source
- Recycled young crust and sediment were involved in the mantle source
- Late Cenozoic magmatism originated from upwelling of the mantle transition zone

Supporting Information:

Supporting Information may be found in the online version of this article.

Correspondence to:
S. Qian and H. Zhou,
shengpingqian@tongji.edu.cn;
zhouhy@tongji.edu.cn

Citation:
Qian, S., Gazel, E., Nichols, A. R. L., Cheng, H., Zhang, L., Salters, V. J., et al. (2021). The origin of late Cenozoic magmatism in the South China Sea and Southeast Asia. *Geochemistry, Geophysics, Geosystems*, *22*, e2021GC009686. https://doi.org/10.1029/2021GC009686

Received 10 FEB 2021
Accepted 23 JUL 2021

The Origin of Late Cenozoic Magmatism in the South China Sea and Southeast Asia

Shengping Qian[1], Esteban Gazel[2], Alexander R. L. Nichols[3], Hao Cheng[1], Le Zhang[4], Vincent J. Salters[5], Jie Li[4], Xiaoping Xia[4], and Huaiyang Zhou[1]

[1]State Key Laboratory of Marine Geology, Tongji University, Shanghai, China, [2]Department of Earth and Atmospheric Sciences, Cornell University, Ithaca, NY, USA, [3]School of Earth and Environment, University of Canterbury, Christchurch, New Zealand, [4]State Key Laboratory of Isotope Geochemistry, Guangzhou Institute of Geochemistry, Chinese Academy of Sciences, Guangzhou, China, [5]Department of Earth Ocean and Atmospheric Science and NHMFL, Florida State University, Tallahassee, FL, USA

Abstract Basaltic lavas sample recycled crustal materials from their mantle source. Constraining the location and residence time of these recycled materials in the mantle is critical to understand global mantle dynamics. In this study, we present new whole-rock major and trace element abundances, Sr-Nd-Mo-Os isotopes, water contents and He isotopes of volcanic glasses, U-Pb ages of zircons, and compositions of melt inclusions, spinels and olivines from the South China Sea (SCS) seamounts lavas. These new data are compared with literature data from intraplate volcanism of similar age from Southeast (SE) Asia. The isotope data of late Cenozoic lavas from the SCS seamounts and SE Asia can be explained by mixing between enriched mantle 2 (EM2) and depleted mid-ocean ridge basalt mantle components. Our data are consistent with the EM2 signature of late Cenozoic lavas derived from recycled young oceanic crust and sediments. The compositions of olivine phenocrysts indicate an olivine-dominated (peridotitic) mantle source. There is currently no evidence for a high-^{3}He/^{4}He mantle plume component beneath the SCS. Our results combined with geophysical data and plate reconstructions suggest that the late Cenozoic magmatism is related to the upwelling of instabilities from the mantle transition zone (MTZ) triggered by a stagnant slab. The SCS seamount lavas sample an enriched MTZ containing young recycled materials, consistent with regional past subduction. Our study provides additional evidence that storage and recycling of crustal materials in or near the MTZ is an important mechanism to develop global mantle heterogeneities sampled by intraplate volcanoes.

1. Introduction

The Earth's mantle, as sampled by oceanic basalts, displays substantial chemical and isotopic variability restricted by a few identifiable isotopic end-member compositions (e.g., Hofmann, 1997; Zindler & Hart, 1986). Entrainment, mixing, and subsequent melting of recycled oceanic and continental components have long been recognized as an important process resulting in the arrays of isotopic signatures observed in oceanic basalts (e.g., Blichert-Toft et al., 1999; Chauvel et al., 2008; Dixon et al., 2002; Hofmann, 1997; Jackson et al., 2007; Kamenetsky et al., 2012; Sobolev et al., 2007; Stracke et al., 2003; Zindler & Hart, 1986). However, the origin, source lithology, and location of these mantle domains are still a matter of debate.

The correlations between the presence of extreme enriched mantle (EM) or HIMU (high μ = high U/Pb) compositions at hotspots and seismically detected African and Pacific large low-shear velocity provinces suggest that these domains may be located in the deep mantle (Jackson et al., 2018). Some geochemical signatures, such as high crystallization temperatures (Coogan et al., 2014; Putirka, 2008; Trela et al., 2017), high Fe/Mn (Humayun et al., 2004), high ^{186}Os/^{188}Os (Brandon & Walker, 2005), and low ^{182}W/^{184}W (Mundl et al., 2017; Rizo et al., 2019) in plume-derived lavas, have been used to infer an origin from recycled materials and/or from a presumably ancient reservoir in the lower mantle, perhaps in contact with the Earth's core. Nevertheless, besides these deep-mantle reservoirs, it is still possible that other shallow boundary layers participate in the generation and evolution of mantle components sampled by intraplate volcanoes (Anderson, 2001).

The distribution of crustal materials in the mantle, the location of these reservoirs, and the timescales of recycling are important parameters necessary for the understanding of global mantle circulation and possible

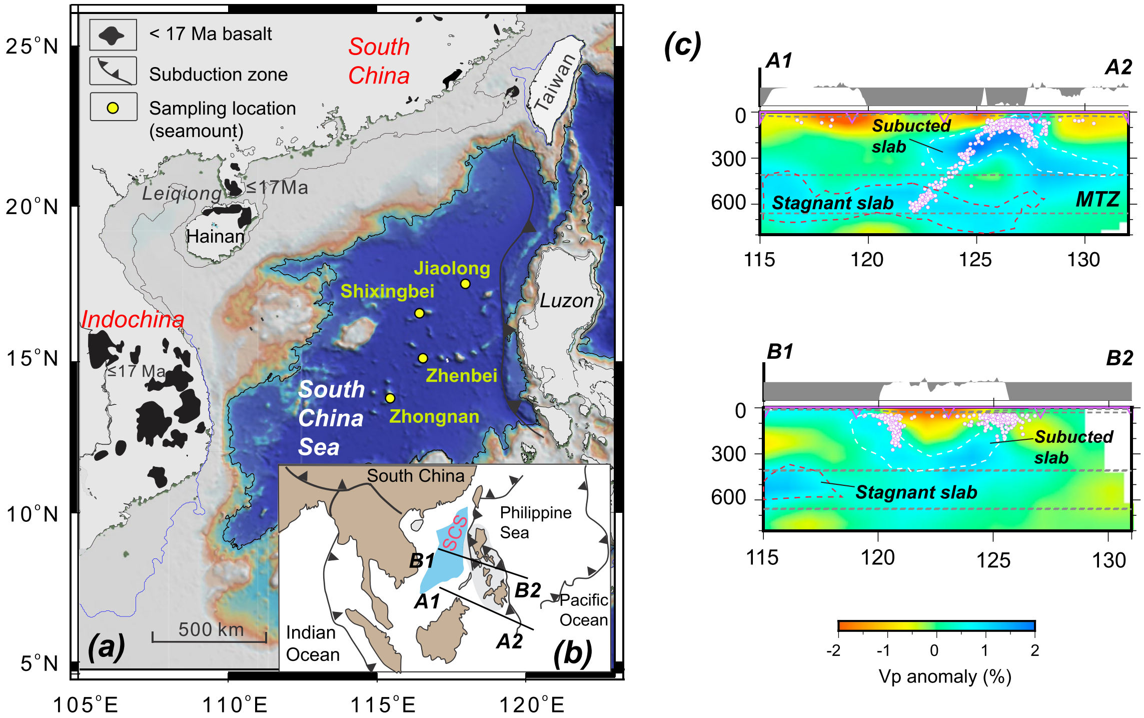

Figure 1. (a) Geological and bathymetric map of the South China Sea (SCS) and adjacent regions. Bathymetric data from GEBCO_2014 Grid (http://www.gebco.net). Distribution of late Cenozoic (<17 Ma) intraplate volcanism in the SCS basin and Southeast (SE) Asia (including SE China, Vietnam, and Thailand) (X. C. Wang et al., 2013; Yan et al., 2008). (b) Inset map showing location of tomographic profiles. (c) Cross section of *P* wave velocity tomography along profile A1–A2 and B1–B2 in (b) beneath SE Asia (Huang et al., 2015).

upwelling mechanisms from different boundary layers (Blichert-Toft et al., 1999; Chauvel et al., 1992; Dale et al., 2009; Konter & Becker, 2012; Mather et al., 2020; Mazza et al., 2019; Qian, Nichols, et al., 2020; Sobolev et al., 2011; Stracke et al., 2003). For example, deep and ancient recycling near the core-mantle boundary has been conventionally proposed for the generation of extreme isotopic mantle end members (e.g., Blichert-Toft et al., 1999; Hofmann, 1997). Alternatively, seismic and experimental studies coupled with the discovery of deep diamond inclusions (Pearson et al., 2014; Tschauner et al., 2018) provide evidence of recycled materials also being stored in the mantle's transition zone. Thus, knowledge of the role of these different boundary layers in the generation of mantle heterogeneity is critical to understanding mantle evolution and dynamics.

The South China Sea (SCS) formed as a result of continental rifting and seafloor spreading (C.-F. Li, Xu, et al., 2014). After seafloor spreading ceased (~16 Ma), small-volume of geochemically enriched post-spreading eruptions occurred across the SCS Basin and surrounding area (An et al., 2017; Gu et al., 2019; Ho et al., 2003; N. Hoang et al., 1996; T. H. A. Hoang et al., 2018; J. Q. Liu et al., 2015; Nguyen et al., 1996; Tu et al., 1992; X. C. Wang et al., 2012; Yan et al., 2008; G.-L. Zhang et al., 2017; Zou & Fan, 2010) (Figure 1). The nature of these lavas has been explained by sampling different potential sources: (a) recycled subcontinental lithospheric mantle (SCLM) or delaminated lower crust (e.g., N. Hoang et al., 1996; Qian, Zhou, et al., 2020; G.-L. Zhang, Luo, et al., 2018; L. Zhang, Ren, et al., 2018; Zou & Fan, 2010); (b) the Hainan mantle plume in the northern SCS with an EM 2 (EM2) type composition (e.g., Gu et al., 2019; Tu et al., 1992; X. C. Wang et al., 2013; G.-L. Zhang, Luo, et al., 2018; L. Zhang, Ren, et al., 2018); or (c) an influx of Indian mid-ocean ridge basalt (MORB)-mantle as a result of the northern movement of Australian Plate (Hickey-Vargas et al., 1995).

To better understand the origin of mantle heterogeneities sampled by late Cenozoic volcanism in the SCS and SE Asia, and the potential location and spatial distribution of isotopically distinct geochemical reservoirs, we present new U/Pb ages on zircons and comprehensive geochemical data of volcanic glasses, melt inclusions, spinels and olivines, as well as host whole-rock data of SCS seamounts lavas (Figure 1).

2. Geological Setting and Samples

The SCS, one of the largest marginal seas in the western Pacific (~3.5×10^6 km^2), is located in the confluence of three major tectonic plates (Pacific-Philippine Sea, Indo-Australian, and Eurasian) (Figure 1). Geophysical evidence shows that the Indian (Burma) Plate subducted along the Sumatra and Java trenches toward the SCS (Figure 1) to a depth of 570–680 km (Hayes et al., 2018) or 800–1,200 km (C. Li et al., 2008). Meanwhile, tomography studies reveal that the Philippine Sea Plate is subducting westward beneath the SCS to a depth of at least 600 km (C. Li et al., 2008). As a consequence, the SCS-mantle dynamics are strongly influenced by the surrounding subduction systems of the Pacific-Philippine Sea and Indo-Australian plates (Figure 1).

Constrained by the combination of recently acquired magnetic anomalies revealed by deep tow and paleomagnetic data from IODP Expedition 349 in the SCS (C.-F. Li, Xu, et al., 2014), seafloor spreading occurred during the early Oligocene to middle Miocene (32–15 Ma). Post-spreading intra-plate volcanoes are a prominent feature in Southeast (SE) Asia (Figure 1). These include continental intraplate lavas found in the SE China (e.g., Leiqiong area), Vietnam, Thailand, and seamount lavas in the SCS Basin (Figure 1). In general, these lavas in SE Asia have similar geochemical characteristics and share common mantle sources as traced by radiogenic isotopes (e.g., N. Hoang et al., 1996; Qian, Zhou, et al., 2020; Tu et al., 1992; X. C. Wang et al., 2013).

The samples in this study were collected from Jiaolong, Shixingbei, Zhongnan, and Zhenbei seamounts located at 1,186–3,493 m below sea level in the SCS (Figure 1). Most lavas from these seamounts display columnar jointing (Figure 2a) and pillow structures (not shown). Glass samples were collected from the Jiaolong and Shixingbei seamounts (Figure 2b). Typically, mafic lavas are vesicular and porphyritic with phenocrysts of olivine, clinopyroxene, and plagioclase (Figures 2c and 2d). Euhedral spinel inclusions and melt inclusions are common in the olivine crystals (Figures 2c and 2e). While felsic lavas (trachytes) are generally phyric with alkali-feldspar, clinopyroxene, and biotite phenocrysts (Figure 2f).

3. Analytical Methods

3.1. Whole-Rock Major and Trace Elements, and Sr-Nd Isotopes

To ensure the best possible analytical quality, the freshest parts of the rocks, identified under a microscope, were used for analytical work. Whole-rock major element compositions were determined on fused glass discs using a PANalytical Axios X-ray fluorescence spectrometer in the State Key Laboratory of Marine Geology (SKLMG) at Tongji University. The glass discs for the analyses were made of a mixture consisting of 0.5 g of sample and 5 g of lithium tetraborate flux ($Li_2B_4O_7$) fused at 1050°C. The loss on ignition of sample powders was determined at a temperature of 1000°C. Analytical procedures are the same as described by C.-Y. Lee et al. (1997). The measurements were monitored using reference materials AGV-1 and BHVO-1 (Table S1).

Trace element concentrations were measured using an inductively coupled plasma-mass spectrometer (ICP-MS) (Perkin-Elmer Sciex ELAN 6000 instrument) after acid digestion of samples in high-pressure Teflon bombs in the Guangzhou Institute of Geochemistry, Chinese Academy of Science (GIGCAS) following analytical procedures described by X.-H. Li et al. (2006). Teflon beakers were cleaned by boiling in HNO_3, HCl, HNO_3 solution (trace metal grade for all acids) and ultrapure water (18.2 MΩ.cm), alternately, with the temperature of 130°C for a 12-h duration in each reagent. For trace element analyses, about 50 mg of sample powder was digested on the hot plate in concentrated HF-HNO_3 on a hotplate at 130°C in beakers for the samples, and then dissolved in concentrated HF-HNO_3-$HClO_4$ at 190°C in steel-jacketed high-pressure Teflon bombs. Procedural blanks were measured together with the samples, which were negligible compared to the concentrations analyzed in the studied samples. The standards BHVO-2 and W-2a were also analyzed along with samples and the analytical precision is generally better than 5% (Table S1).

Sr-Nd isotopic ratios were measured using a Thermo Fisher Scientific Neptune Plus multi-collector (MC)-ICP-MS in the SKLMG at Tongji University. Prior to digestion in concentrated HF-HNO_3 acids, rock powders were leached with 6N HCl at 150°C for 3 days and then triple rinsed in deionized water to remove potential seawater alteration contamination. Duplicate analyses of Sr isotope were conducted for one sample leached

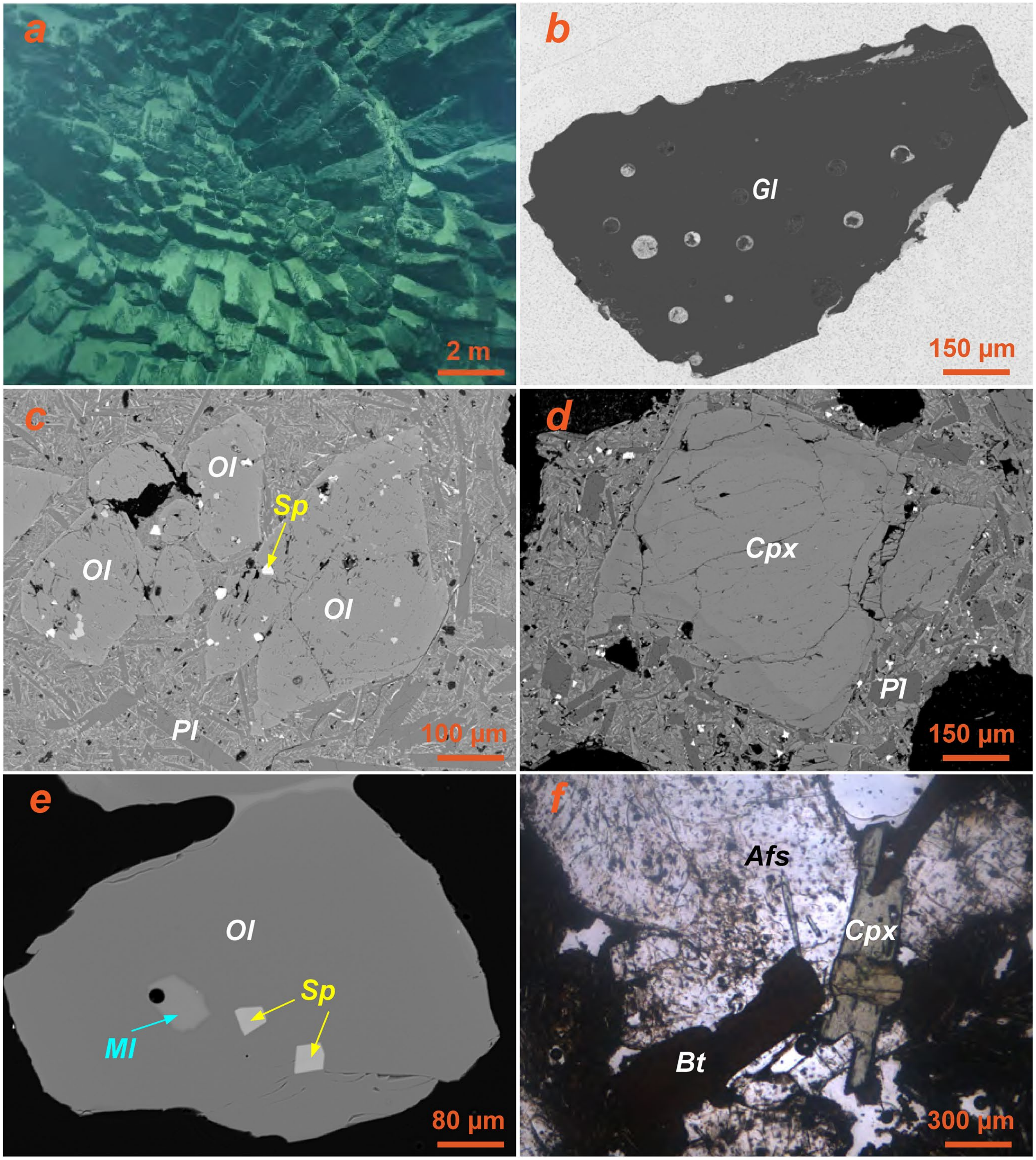

Figure 2. (a) Zhongnan seamount lavas with columnar jointing. (b) Back-scattered electron photograph of fresh glass (Gl), pits generated by the ion beam during analysis of H_2O (white circles) are also visible. (c) Back-scattered electron photograph showing olivine (Ol) and plagioclase (Pl) phenocrysts, and spinels (Sp) within Ol. (d) Back-scattered electron photograph of a clinopyroxene (Cpx) phenocryst. (e) Back-scattered electron photograph of a melt inclusion (MI) and Sp in Ol exposed on the surface. (f) Photomicrograph showing alkali-feldspar (Afs), biotite (Bt), and Cpx phenocrysts in trachyte.

with 2N HCl to check for seawater alteration. As a result, the measured $^{87}Sr/^{86}Sr$ ratios of prolonged-leached samples (0.703344) are slightly lower compared to the mildly leached rock powders (0.703389). These observations suggest that prolonged acid leaching of the sample powders in hot 6N HCl likely minimize or remove the effects of seawater alteration on Sr isotopes.

The interferences of ^{86}Kr on ^{86}Sr and ^{87}Rb on ^{87}Sr were monitored by measuring ^{83}Kr and ^{85}Rb, and corrected by using $^{86}Kr = 1.50566 \times {}^{83}Kr$, and $^{87}Rb = 0.3857 \times {}^{85}Rb$, respectively (Ma et al., 2013). Isobaric interference from ^{144}Sm on ^{144}Nd was corrected with ^{149}Sm intensity and the natural $^{147}Sm/^{144}Sm$ (0.22332) (Isnard et al., 2005). During the course of isotope analysis, the standards NBS-987 and JNdi-1were used as the drift monitor for the instrument. The measured $^{143}Nd/^{144}Nd$ and $^{87}Sr/^{86}Sr$ ratios were normalized to $^{146}Nd/^{144}Nd = 0.7219$ and $^{86}Sr/^{88}Sr = 0.1194$, respectively (Nier, 1938; Tanaka et al., 2000). The mean $^{87}Sr/^{86}Sr$ values of standard NBS987 and $^{143}Nd/^{144}Nd$ values of standard JNdi-1 were 0.710244 ± 0.000016 (2σ, $n = 16$) and 0.512116 ± 0.000010 (2σ, $n = 15$), respectively. The recommended value of 0.710250 was used to correct for $^{87}Sr/^{86}Sr$ values of all samples. The $^{143}Nd/^{144}Nd$ ratios were normalized to JNDi-1 $^{143}Nd/^{144}Nd = 0.512115$ (Tanaka et al., 2000) for mass fractionation. The Sr-Nd isotope data of the samples along with the reference materials (BHVO-2 and W-2a) are provided in Table S1.

3.2. Mo and Re-Os Isotope of Whole-Rock Samples

Chemical separation and mass spectrometry measurements of Mo isotope were conducted at the State Key Laboratory of Isotope Geochemistry, GIGCAS, following analytical procedures described in J. Li, Liang, et al. (2014). Appropriate sample powders were measured to assured 120 ng of Mo and 120 ng of ^{97}Mo-^{100}Mo double spike solution. The Mo double-spike was added before digestion of bulk rock samples. The samples were digested using 4 mL of HF and 2 mL of HNO_3 in closed beakers at 140°C overnight. Mo separation and purification was achieved using an extraction chromatographic resin of N-benzoyl-N-phenyl hydroxylamine manufactured in-house following the protocols of J. Li, Liang, et al. (2014) and Fan et al. (2020). After the sample matrix and elements with isobaric interferences were removed, Mo isotope measurement was performed on a Thermo-Fisher Scientific Neptune-Plus multi-collector inductively coupled plasma mass spectrometer (MC-ICP-MS) utilizing double-spike analysis to correct for instrumental mass bias. Isotope measurements are made relative to a NIST SRM 3134 standard solution. The external reproducibility of NIST SRM 3134 standard solution is 0.06‰ (2SD, $n = 12$) for the $\delta^{98/95}Mo$ values. USGS rock standard BHVO-2 and IAPSO seawater standard were simultaneously processed with each batch of samples to monitor accuracy and gave the $\delta^{98/95}Mo$ value of −0.04 ± 0.05‰ and 2.06 ± 0.04‰, respectively. These results are consistent with certified values and with the values reported by previous studies (−0.05 ± 0.11‰ for BHVO and 2.09 ± 0.04‰ for IAPSO) (Greber et al., 2012; J. Li, Liang, et al., 2014). The total procedural blank (TPB) for our analyses was 0.66 ± 0.37 ng (2SD, $n = 3$) Mo, far less than the total Mo in the samples (3.22–6.95 μg/g).

Re-Os separation and analyses were performed using the procedures described in J. Li, Zhao, et al. (2015). Bulk powdered samples (~2.5 g) together with solutions enriched in ^{190}Os and ^{185}Re were digested in inverse aqua regia in sealed Carius tubes at 240°C for at least one day. Os was extracted by CCl_4 and then extracted back into high-purity concentrated HBr. Further purification of Os was accomplished via micro-distillation. Re was recovered and purified from the solution in anion exchange columns (AG1 × 8, 200–400 resin).

Os was loaded onto Pt filaments and measured as OsO_3^- ions by negative thermal ionization mass spectrometry using secondary electron multiplier in single collector peak hopping mode on a Thermo-Finnigan Triton at the State Key Laboratory of Isotope Geochemistry, GIGCAS. Repeated analyses of the Os standard solution (Merck Chemical AA standard solution) yield a mean $^{187}Os/^{188}Os$ value of 0.12045 ± 0.00042 (2 SD, $n = 6$) for the period of analysis. These values are in good agreement with a value of 0.12022 ± 0.00020 (2 SD, $n = 14$) measured on the same mass spectrometer in Faraday cup mode (J. I. E. Li et al., 2010). Instrumental mass fractionation corrections for Os measurements were performed by normalizing the measured $^{192}Os/^{188}Os$ to 3.083. Rhenium concentration was analyzed by inductively coupled plasma mass spectrometry (Thermo Elemental X2 Series).

TPBs were 0.52 ± 0.24 pg (1σ, $n = 2$) with an $^{187}Os/^{188}Os$ ratio of 0.13 ± 0.24 (1σ, $n = 2$) on average for Os and 2.9 ± 0.1 pg (1σ, $n = 2$) for Re. All data were corrected for the procedural blank for each analytical batch. Blank contributions were generally insignificant. The average values of Re-Os isotope for basaltic reference material BIR-1 ($^{187}Os/^{188}Os = 0.13340 \pm 0.00024$, Os = 0.351 ± 0.032 ppb, Re = 0.676 ± 0.016 ppb, 1σ, $n = 2$) are in good agreement with published data ($^{187}Os/^{188}Os = 0.13369–0.13372$, Os = 0.341–0.355, Re = 0.675–0.680) (Ishikawa et al., 2014; J. Li, Wang, et al., 2015).

3.3. In Situ U-Pb Dating Analyses of Zircon

Three lavas samples (one trachyandesite 2059-R12 from the Zhenbei seamount and two evolved trachytes 2056-R10 and 2056-R14 from the Zhongnan seamount) were used for U-Pb zircon dating. Cathodoluminescence (CL) images were taken for all zircons at the SKLMG in Tongji University, China. Zircon U-Pb dating was carried out by LA-ICP-MS (a RESOlution M-50 laser ablation system coupled to a Thermo Element 2 instrument) at GIGCAS, China. For details of operating conditions for the laser ablation system and the ICP-MS instrument and data reduction, refer to G.-L. Zhang, Luo, et al. (2018) and L. Zhang, Ren, et al. (2018). Each analysis spot was about 33 μm in diameter and the repetition rate was 5 Hz. Each analysis incorporated a background acquisition of 30 s (gas blank) followed by 40 s data acquisition from the sample. In order to monitor the external uncertainties of U-Pb zircon measurements, the zircon standards 91500 and Plešovice were analyzed as calibration standard and monitor standard, respectively. Common Pb was corrected using the Excel program ComPbCorr#_151 (Andersen, 2002). Off-line isotopic ratio calculations were performed using software GLITTER. During our measurement, 20 analyses of Plešovice yield an averaged $^{206}Pb/^{238}U$ age of 338.4 ± 3.5 Ma, agreeing with the reference value within analytical error (Sláma et al., 2008). Meanwhile, the standard zircon 91500 yielded a weighted $^{206}Pb/^{238}U$ age of 1061.5 ± 3.8 Ma (2σ, $n = 10$), which is identical within error with the recommended value of 1062.4 ± 0.4 Ma (Wiedenbeck et al., 1995).

3.4. He Isotope Analyses of Glasses

He isotopes ratios were measured on glasses separated from six volcanic rocks at the Helium Isotope Laboratory, NOAA Pacific Marine Environmental Laboratory, Newport, Oregon (Table S2). For He analysis, small chips of glass from the chilled margin of lavas were selected to minimize the occurrence of phenocrysts and optimize their purity. Then, the glass chips (weighing 0.1–0.6 g) were cleaned in distilled water and acetone, and loaded into stainless steel "crusher" tubes (Lupton et al., 2015). The detailed operating conditions, and analytical procedures are provided in Lupton et al. (2015). Blanks were run on each of the loaded tubes before proceeding with mass spectrometry, with blanks averaging at 1.2×10^{-10} cc STP He. The precision for the He isotope analysis on glass samples averaged about 0.15 Ra.

3.5. H_2O Abundance Analyses of Glasses

H_2O abundances of volcanic glasses were analyzed by the CAMECA IMS 1280-HR ion microprobe at GIGCAS. Detailed analytical procedures specifically for hydrogen measurements with this instrument were developed by X.-P. Xia et al. (2019) and W.-F. Zhang et al. (2020). The glass samples were sputtered with a 10 kV $^{133}Cs^+$ primary beam (1.5–3.2 nA) and $\phi \sim 15$ μm, with an impact energy of 10 kV to sputter secondary ions from the samples. The size of the analytical area was 30 × 30 μm (15 μm spot size + 15 μm rastering). To minimize H_2O backgrounds, the instrument was baked for at least 24 h and an automatic liquid nitrogen refilling system was used to yield ultra-high vacuum conditions. Samples were mounted on tin-based alloy mount and stored under vacuum for at least 6 h prior to analysis (W.-F. Zhang et al., 2020). A normal-incidence electron gun was used for sample charge compensation during the course of analysis and the nuclear magnetic resonance controller was used to stabilize the magnetic field. After pre-sputtering (170 s), the intensities of $^{16}O^-$, $^{18}O^-$, and $^{16}O^1H^-$ secondary ions were simultaneously measured. Two Faraday cup detectors with 10^{10} Ω and 10^{11} Ω amplifiers, and a single electron multiplier were used for static measurement of $^{16}O^-$, $^{18}O^-$, and $^{16}O^1H^-$, respectively. The relative signal intensity of $^{16}O^1H$ to ^{16}O with a calibration curve of three well-characterized hydrous glass standards was used to yield estimates of water content for each spot analysis. The hydrogen background during the analyses was on the order of 10 ppm (X.-P. Xia et al., 2019; W.-F. Zhang et al., 2020). To monitor accuracy and repeatability of H_2O content analysis, BCR-2G and MORB glass were repeatedly analyzed during the analytical session (Table S7).

3.6. In Situ Major and Trace Element Analyses of Minerals and Glasses

Major element analyses of olivine, spinel, melt inclusion, and glass were performed on a JEOL JXA-8230 electron probe micro-analyzer (EPMA) at the SKLMG, Tongji University. The operating conditions for olivine were a 20 kV accelerating voltage and a 100 nA beam current, and a 15 kV accelerating voltage and a 20 nA beam current for spinel, melt inclusions and glasses. A variable peak counting time of 10–120 s was designed for the intensity of the characteristic X-ray lines and desired precision. A range of metal, oxide and silicate (e.g., jadeite, wollastonite) standards (e.g., jadeite for Na, periclase for Mg, wollastonite for Ca, Si, rutile for Ti, fayalite for Fe, K-feldspar for K, corundum for Al, apatite for P, manganotantalite (Mn) and pure metals for Cr, and Ni) were used to calibrate the spectrometers and for matrix reduction of the data. During the measurement of olivine, the San Carlos olivine standard was used to monitor the accuracy of the measurements (Table S7).

In situ trace element analyses of olivines and volcanic glasses were carried out by LA-ICP-MS using an excimer 193 nm laser ablation system (GeoLas 2005) in combination with an Agilent 7500 ICP-MS instrument at the GIGCAS. The carrier and make-up gas flows were optimized by ablating NIST SRM 610 to acquire maximum signal intensity for ^{208}Pb, while maintaining low ThO/Th (<0.3%) and Ca^{2+}/Ca^{+} ratios (<0.5%) to reduce interferences of oxides, argides and doubly charged ions as much as possible (L. Zhang et al., 2019). The laser parameters were set as following: spot size, 45 μm; repetition rate, 6 Hz; energy density, ~4 J cm^2. Each spot analysis consisted of 30 s gas blank collection with laser off and 50 sample signal collection with laser on. A previous study (Y. Liu, Hu, et al., 2008) show insignificant matrix effect between olivine and basaltic glass. In addition, the trace elements we concerned in olivine have similar levels of concentrations in both the standard BHVO-2G and BCR-2G. Therefore, the USGS standard glass GSD-1G was used as the external calibrator. Si content, measured by EPMA, was used for internal standardization. The detailed operating conditions for the laser ablation system and ICP-MS instrument are provided in L. Zhang et al. (2019). The analytical precision generally was better than 10% for the standards BCR-2G and BHVO-2G (Table S7).

4. Results

4.1. Whole-Rock Compositions

The lavas analyzed in this study from the SCS seamounts have SiO_2 values between 45.49 and 63.10 wt.% (Figure 3). Zhongnan and Zhenbei lavas belong to the alkaline series and are primarily basanite and trachybasalt with one trachyandesite and several evolved trachytes, while Jiaolong and Shixingbei lavas plot in the tholeiitic basalt field (Figure 3a). The Zhongnan and Zhenbei alkaline lavas have higher alkalis ($Na_2O + K_2O$) (4.79–12.35 wt.%), Al_2O_3 (14.66–18.42 wt.%) and TiO_2 (0.54–3.68 wt.%), and lower CaO (1.28–10.42 wt.%) than Jiaolong and Shixingbei subalkaline lavas at a given MgO (Figure 3).

When normalized to primitive mantle (Figure 4a), the SCS seamount lavas show enrichments in incompatible elements, and positive anomalies of Nb and Ta. Some seamount lavas are characterized by pronounced troughs in Sr and Ti (Figure 4a). In general, the Jiaolong and Shixingbei tholeiitic basalts have much lower incompatible trace element concentrations than the Zhongnan and Zhenbei lavas (Figure 4a). Notably, Jiaolong tholeiitic basalts have significantly lower concentrations of incompatible trace element than the other seamount lavas, similar to MORBs erupted during the SCS spreading stage (Figure 4a). The SCS seamount lavas show a large variation in La/Sm (2.31–10.0), Sm/Yb (0.93–3.89), and Nb/U (26.6–57.2) (Figures 4b–4d).

$^{87}Sr/^{86}Sr$ and $^{143}Nd/^{144}Nd$ of lavas from the SCS seamounts are variable (Figure 5). The Jiaolong and Shixingbei tholeiitic basalts have lower $^{87}Sr/^{86}Sr$ (0.703121–0.703344) and higher $^{143}Nd/^{144}Nd$ (0.512916–0.513082) than the Zhongnan and Zhenbei lavas (0.703387–0.704732 for $^{87}Sr/^{86}Sr$ and 0.512686–0.512977 for $^{143}Nd/^{144}Nd$) (Figure 5). The Jiaolong tholeiitic basalts are similar to the MORBs erupted during the SCS spreading stage in their Sr-Nd isotope compositions; whereas Sr-Nd isotope compositions of some Zhongnan and Zhenbei lavas tend toward an EM component (Figure 5). These data combined with published Sr-Nd-Pb data for the lavas in the SCS and surrounding area primarily plot between the depleted MORB mantle (DMM) and EM2 mantle end-members (Figures 5 and S9).

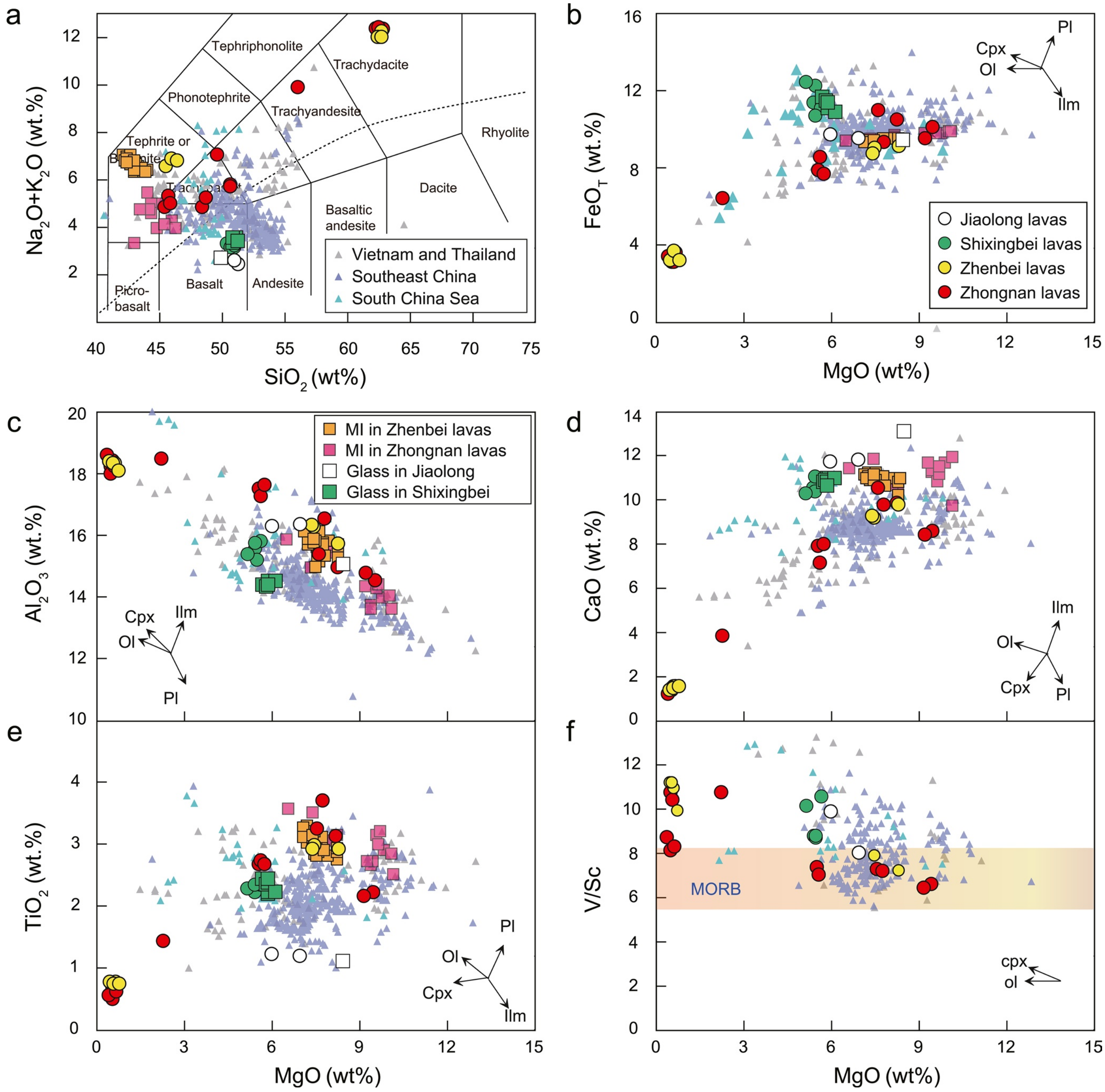

Figure 3. Variation of major and minor element for whole rock, melt inclusion and glass from the South China Sea (SCS) seamounts Zhongnan, Zhenbei, Jiaolong, and Shixingbei. (a) Total alkali content ($Na_2O + K_2O$) versus SiO_2, (b–f) FeO, Al_2O_3, CaO, TiO_2, V/Sc versus MgO. Data for late Cenozoic lavas in the SCS and Southeast (SE) Asia (including SE China, Vietnam, and Thailand) are from the GEOROC database (http://georoc.mpchmainz.gwdg.de/georoc). Major element contents are normalized to 100% on a volatile-free basis. The V/Sc range of mid-ocean ridge basalt is from C.-T. A. Lee et al. (2005). Cpx, clinopyroxene; Ol, olivine; Pl, plagioclase.

The SCS seamount lavas have much higher Mo contents (3.22–6.95 ppm) (Table S1) than those of MORB (average 0.48 ± 0.13 ppm) (Liang et al., 2017); the $\delta^{98/95}Mo$ vary between −0.15 and −0.49 (Figures 5b and 5c), which is significantly lower than that of MORB (Figures 5b and 5c). The $\delta^{98/95}Mo$ of SCS seamount lavas decrease with increasing $^{87}Sr/^{86}Sr$ and decreasing $^{143}Nd/^{144}Nd$ (Figures 5b and 5c). The SCS seamount lavas have a large range of $^{187}Os/^{188}Os$ from 0.1303 to 0.1490 (Figure 5d). Os concentrations range from 0.06 to 0.20 ppb and Re concentrations vary from 0.046 to 0.15 ppb (Table S1). $^{187}Re/^{188}Os$ range from 0.62 to 12.1 (Table S1). The Os isotope ratios are similar to those of previous results (0.1227–0.1829) for southern China

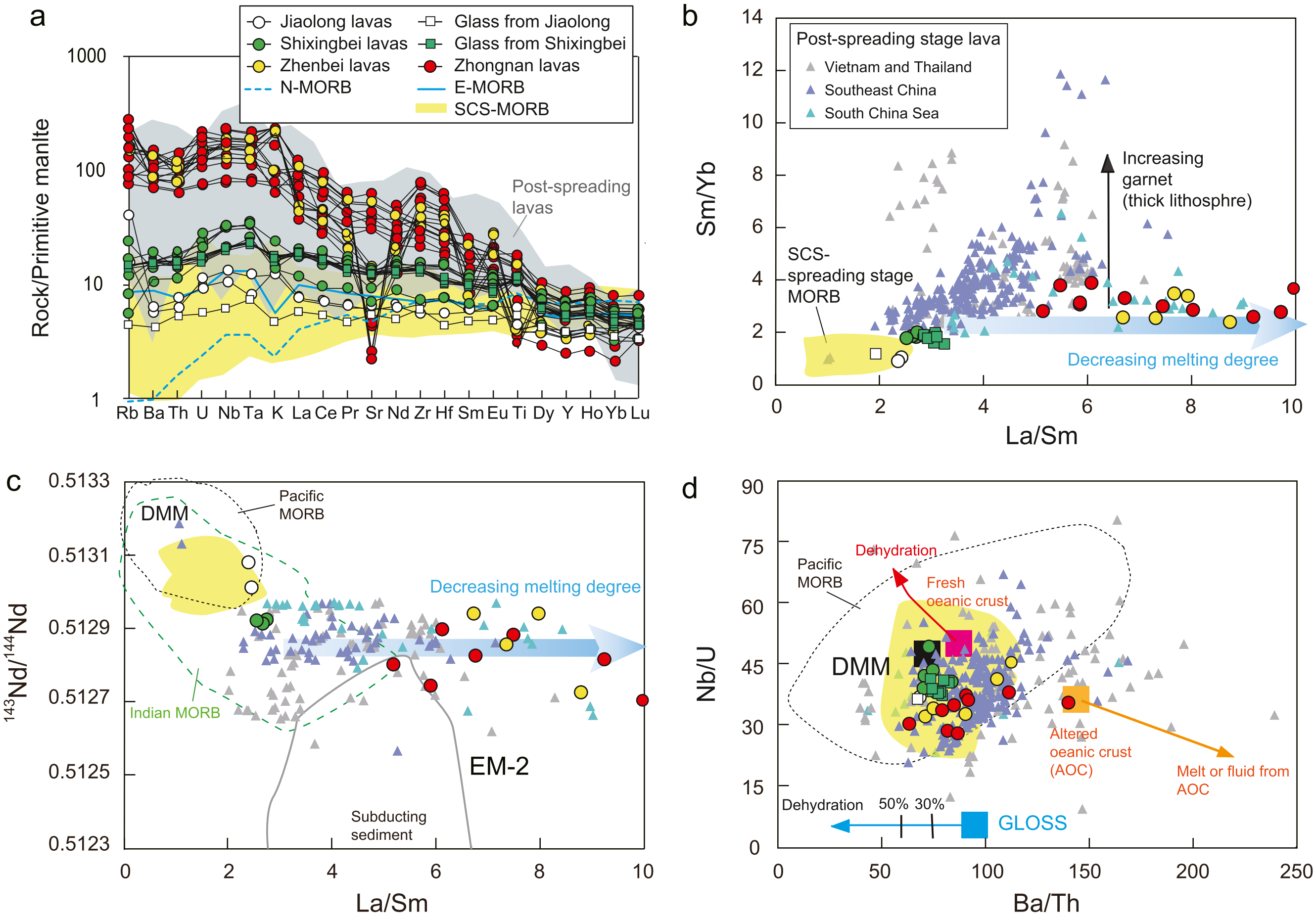

Figure 4. (a) Primitive mantle-normalized multi-element diagram for whole rock and glass from the South China Sea (SCS) seamounts Zhongnan, Zhenbei, Jiaolong, and Shixingbei. (b) La/Sm versus Sm/Yb. (c) ^{143}Nd/^{143}Nd versus La/Sm. (d) Ba/Th versus Nb/U. Variations in Nb/U and Ba/Th ratios during dehydration of recycled crustal materials are calculated following Pietruszka et al. (2013). Primitive mantle, N-mid-ocean ridge basalt (MORB), and E-MORB (Sun & McDonough, 1989), the SCS spreading stage MORB (G.-L. Zhang, Luo, et al., 2018; L. Zhang, Ren, et al., 2018), late Cenozoic lavas in the SCS and Southeast Asia from the GEOROC database (http://georoc.mpch-mainz.gwdg.de/georoc), the trace-element ratios and Sr-Nd isotopes for Pacific and Indian MORBs (Stracke, 2012), fresh or altered oceanic crust (Pietruszka et al., 2013; Sun & McDonough, 1989), and sediments (Plank & Langmuir, 1998) are shown for comparison. DMM, depleted MORB mantle; EM2, enriched mantle 2.

(e.g., Hainan) basalts in the northern SCS and are higher than most SCLM peridotites and MORBs (C.-Z. Liu, Snow, et al., 2008; Meisel et al., 2001) (Figure 5d).

4.2. Glasses and Melt Inclusions

Volcanic glasses from the Jiaolong and Shixingbei seamounts are similar in composition to lavas from the same seamounts collected in this study, plotting in the tholeiitic basalt field (Figure 3a). The volcanic glasses have moderate MgO (5.76–8.49 wt.%), FeOt (9.37–11.54 wt.%) and Al_2O_3 (14.33–15.02 wt.%), relatively high CaO (10.72–12.98 wt.%), and low total alkalies (2.58–3.52 wt.%), and TiO_2 (1.10–2.40 wt.%) (Figure 3). Major element oxides, such as Al_2O_3 and CaO, show positive correlations with MgO, while TiO_2 and FeOt yield negative correlations (Figure 3).

Melt inclusions in olivines from the SCS seamount lavas after corrections for post-entrapment modifications (see supplementary materials for details) have moderate MgO (5.76–8.49 wt.%), FeOt (9.37–11.54 wt.%) and Al_2O_3 (14.33–15.02 wt.%), relatively high CaO (10.72–12.98 wt.%), and low total alkalies (2.58–3.52 wt.%), and TiO_2 (1.10–2.40 wt.%). Al_2O_3 and total alkalies of the SCS seamount melt inclusions largely show negative correlations with MgO (Figure 3). Therefore, melt inclusion compositions record liquid lines of descent that are controlled by olivine fractionation and are consistent with the whole-rock compositions (Figure 3).

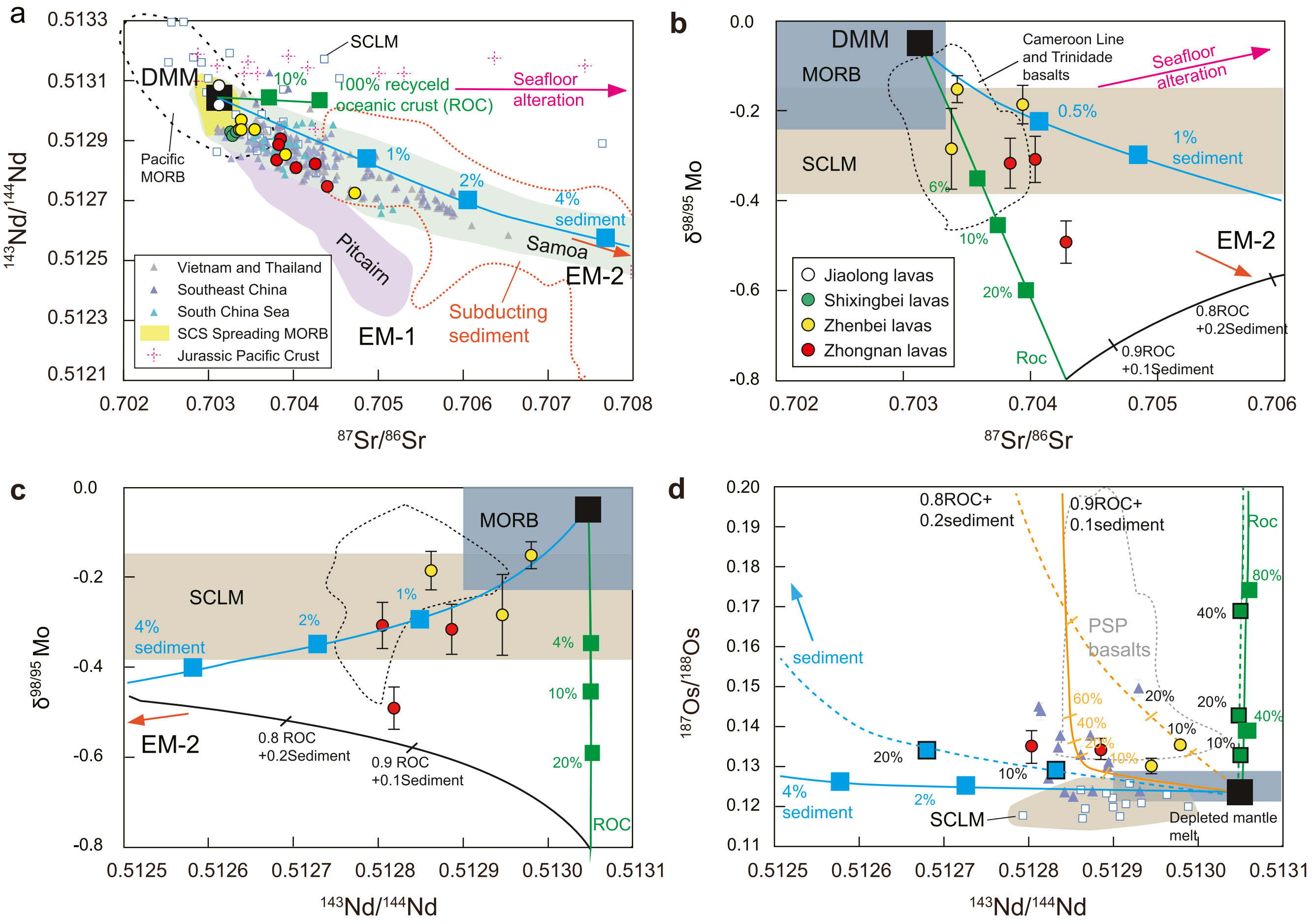

Figure 5. Isotopic compositions of the South China Sea (SCS) seamounts lavas. (a) Variation of ^{87}Sr/^{86}Sr versus ^{143}Nd/^{143}Nd, (b) δ$^{98/95}$Mo versus ^{87}Sr/^{86}Sr, (c) δ$^{98/95}$Mo versus ^{143}Nd/^{143}Nd, and (d) ^{187}Os/^{188}Os versus ^{143}Nd/^{143}Nd. The modeling results (those presented here are not unique) show mixing trends between depleted end-component (depleted MORB mantle [DMM]) and recycled oceanic crust and sediments. Data used for mixing calculation are as follows: DMM (^{87}Sr/^{86}Sr = 0.7031, ^{143}Nd/^{143}Nd = 0.51304, δ$^{98/95}$Mo = −0.05, ^{187}Os/^{188}Os = 0.125, Sr = 9.8 ppm, Nd = 0.83 ppm, Mo = 0.03 ppm, Os = 3 ppb) (Bezard et al., 2016; Gannoun et al., 2007; Workman & Hart, 2005; G.-L. Zhang, Luo, et al., 2018; L. Zhang, Ren, et al., 2018), recycled oceanic crust (^{87}Sr/^{86}Sr = 0.70429, ^{143}Nd/^{143}Nd = 0.51305, δ$^{98/95}$Mo = −0.8, ^{187}Os/^{188}Os = 0.5, Sr = 98.5 ppm, Nd = 8.3 ppm, Mo = 0.31 ppm, Os = 0.05 ppb) (Freymuth et al., 2015; Hauff et al., 2003; Hofmann, 1988; Peucker-Ehrenbrink et al., 2012), sediment (^{87}Sr/^{86}Sr = 0.71236, ^{143}Nd/^{143}Nd = 0.51221, δ$^{98/95}$Mo = −0.45, ^{187}Os/^{188}Os = 0.6, Sr = 222 ppm, Nd = 24.8 ppm, Mo = 5 ppm, Os = 0.1 ppb) (Gaschnig et al., 2017; Peucker-Ehrenbrink et al., 1995; Plank & Langmuir, 1998); dashed line showing mixing between depleted peridotite-derived melts (Os = 0.5 ppb, Nd = 8.0 ppm), and partial melts of recycled oceanic crust (Os = 0.05 ppb, Nd = 8.3 ppm) and recycled sediment (Os = 0.1 ppm, Nd = 24.8 ppm). Sources of data: Sr and Nd isotopes of the SCS spreading stage mid-ocean ridge basalt (MORB)-type lavas from G.-L. Zhang, Luo, et al. (2018) and L. Zhang, Ren, et al. (2018), Pacific MORBs from Stracke (2012), and Jurassic Pacific crust from Hauff et al. (2003), subcontinental lithospheric mantle (SCLM) represented by the lithospheric mantle xenoliths beneath Southeast (SE) China from C.-Z. Liu, Snow, et al. (2008), Tatsumoto et al. (1992), and Xu et al. (2003); Mo isotope of typical MORB from Bezard et al. (2016) and Liang et al. (2017), typical continental intraplate basalts (Cameroon Line basalts) and Trinidade basalts from Liang et al. (2017), the lithospheric mantle xenoliths from Liang et al. (2017); Os isotope of Hainan basalts in South China from X. C. Wang et al. (2013), Philippine Sea Plate (PSP) basalts from Dale et al. (2008), the lithospheric mantle xenoliths beneath SE China from C.-Z. Liu et al. (2017), MORB from Gannoun et al. (2007). The detailed references for the published data of lavas from the SCS and SE Asia are provided in the Supporting Information. Data sources for EM1-type (Pitcairn islands) and EM2-type oceanic island basalts (Samoa islands) have been compiled by Stracke et al. (2003). The error bars correspond to 2 standard error (2 SE).

The volcanic glasses from the SCS seamounts have H_2O contents of 0.22–0.79 wt.%, and H_2O/Ce of 242–282 (Figures 6a, 6b and S1). The measured H_2O contents and H_2O/Ce of the SCS seamount volcanic glasses are largely similar to those for the primary melts of the Hainan basalts (0.28–1.24wt.% for H_2O contents and 50–319 for H_2O/Ce; Gu et al., 2019) in southern China, to the north of the SCS (Figures 6a and 6b).

The ^{3}He/^{4}He isotopic ratios of volcanic glasses in SCS seamounts range from 7.36 to 8.03 R/R_A (Figures 6c and 6d). The most striking feature of these results is that the ^{3}He/^{4}He of the SCS glasses all fall within a relatively narrow range of ambient mantle MORBs (Figures 6c and 6d).

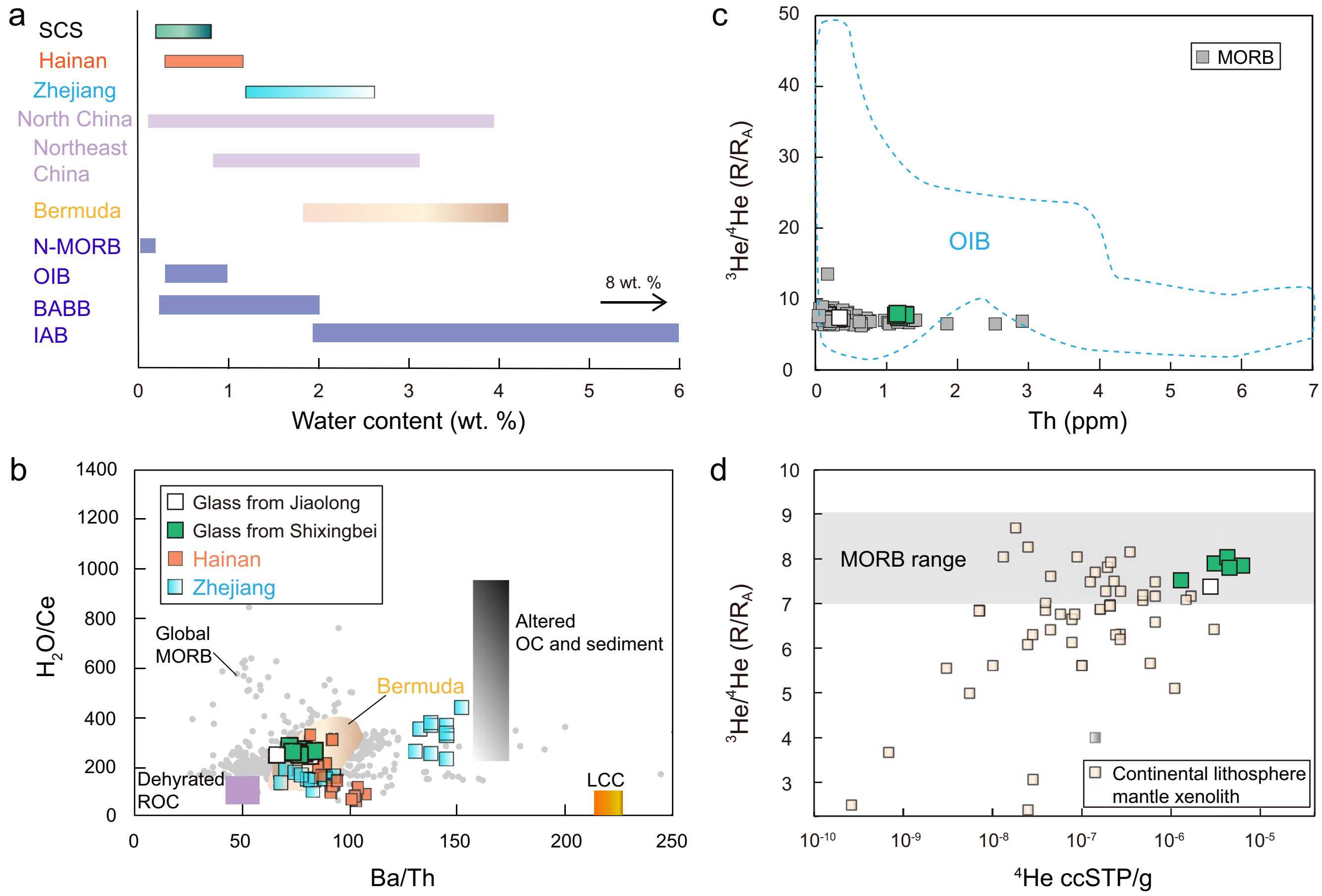

Figure 6. Compositions of volcanic glasses from the South China Sea (SCS) seamounts. (a) Comparison of water contents in the SCS seamount volcanic glasses with those from different geological settings. The water contents of the Hainan basalts (Gu et al., 2019), Zhejiang basalt (S.-C. Liu et al., 2016), North and Northeast China basalts (Q. K. Xia et al., 2017), Bermuda lavas (Mazza et al., 2019), oceanic island basalt (OIB), normal mid-ocean ridge basalt (MORB), back-arc basin basalt (BABB), and island arc basalt (IAB) (Dixon et al., 2004) are included for comparison. (b) H_2O/Ce versus Ba/Th. Rectangles show the possible mantle source end members. H_2O/Ce for lower continental crust (LCC) (<50), and recycled altered and dehydrated oceanic crust and sediments are from Dixon et al. (2002), X. Z. Yang et al. (2008), and references therein. Ba/Th for depleted MORB mantle, LCC, and recycled dehydrated and altered oceanic and sediments are from Workman and Hart (2005), Rudnick and Gao (2003), and Plank and Langmuir (1998). H_2O/Ce and Ba/Th of Bermuda lavas and global MORB are from Mazza et al. (2019) and Le Voyer et al. (2019), respectively. (c) $^3He/^4He$ verus Th, (d) $^3He/^4He$ verus ^4He of glasses from the SCS seamounts. The data for OIB, MORB, and continental lithosphere mantle xenoliths are shown for comparison (Class & Goldstein, 2005; Day et al., 2005).

4.3. Olivine and Spinel

Olivines from the SCS seamount lava show a relatively large range of Fo contents (80.3–86.8) (Figure 7). Their Fo contents correlate positively with Ni (1,014–2,871 ppm) and Cr (21–366), and negatively with Mn (1,442–2,335 ppm) (Figure 7). No correlation is seen with Ca (893–2,150 ppm), Fe/Mn (53–70), or Ni/(Mg/Fe)/1,000 (0.49–1.02) (Figure 7). As a whole, the SCS seamount olivines have lower Ni, Fe/Mn, Ni/(Mg/Fe)/1,000, and NiO/MnO, and higher Mn than the olivines in SE Asia (e.g., Hainan and Indochina) basalts (Figures 7 and 8).

Spinel inclusions hosted by the olivines are characterized by high Al_2O_3, moderate TiO_2 (0.36–1.82 wt%), and relatively low Cr# (25–45) (Figure S2 and Table S5). Overall, spinel inclusions plot in the compositional range of spinel from volcanic rocks, with higher TiO_2 contents than those from mantle peridotites (Figure S2).

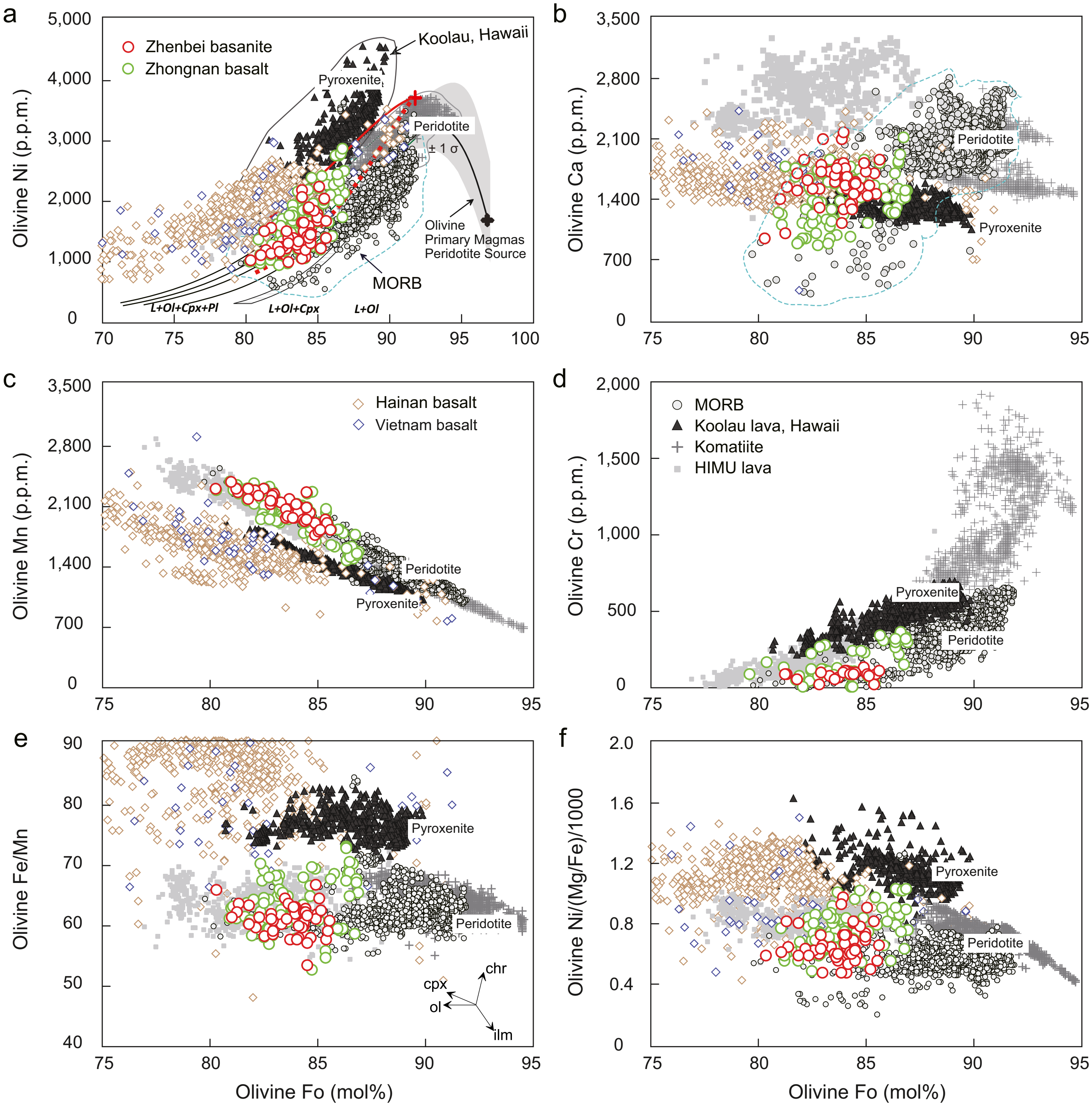

Figure 7. Plots of Mg# versus (a) Ni, (b) Ca, (c) Mn, (d) Cr, (e) Fe/Mn, and (f) Ni/(Mg/Fe)/1,000 in olivines from basalts in the Zhenbei and Zhongnan seamounts. Also shown are data for olivines in lavas from Southeast Asia (An et al., 2017; Gu et al., 2019; T. H. A. Hoang et al., 2018; J. Q. Liu et al., 2015; X. C. Wang et al., 2012), mid-ocean ridge basalt (MORB), Koolau basalts in Hawaii and komatiites (Sobolev et al., 2007), and HIMU basalts (Weiss et al., 2016) for comparison. The black bold curve is the calculated Ni content in olivine crystallized from all primary melts generated from a peridotite source with 1,960 ppm. Ni with the gray field representing ±1σ uncertainty (Herzberg et al., 2014); the black hatched area and black curves denote the calculated Ni content of olivine from olivine fractionated derivative melts from primary magmas (Herzberg et al., 2014). The red solid and dashed lines are for olivine that crystallized from primary magmas (red crosses) generated from Ni-rich fertile peridotite with 2,360 ppm Ni that subsequently fractionated olivine, and olivine and clinopyroxene (30% and 70%) (Herzberg et al., 2014).

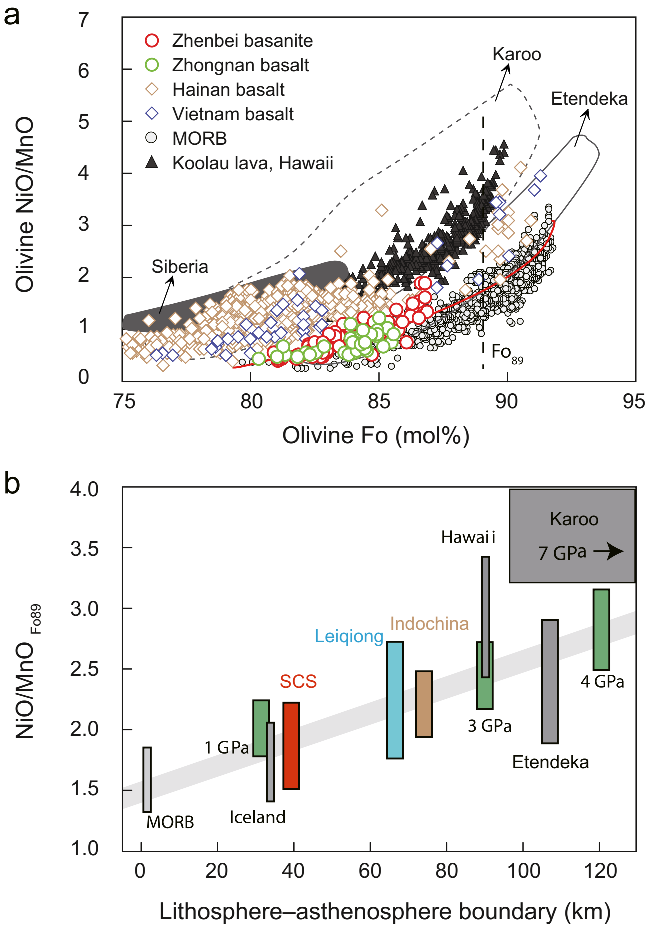

Figure 8. (a) Fo (%) versus NiO/MnO in olivines from the Zhongnan and Zhenbei seamounts. Olivine data for mid-ocean ridge basalt (MORB), Hawaii, and Siberian data are from Sobolev et al. (2007), data source for olivine in late Cenozoic lavas from Southeast Asia are same as Figure 7. (b) NiO/MnO$_{\mathrm{Fo89}}$ (NiO/MnO at olivine Fo contents of 89) for olivines from the South China Sea seamounts, Zhongnan and Zhenbei, versus lithosphere-asthenosphere boundary depth (km) compared to other settings and the 1, 3, and 4 GPa experiments of Matzen, Baker, et al. (2017). The lithosphere-asthenosphere depths for Etendeka and Karoo are compiled from Howarth and Harris (2017), and the MORB, Iceland and Hawaii data were compiled from Sobolev et al. (2007).

4.4. Zircon U-Pb Ages

Zircons are mostly euhedral and prismatic, devoid of discernible inherited cores, and display igneous oscillatory zoning under cathodoluminescence (CL) (Figure S3). Zircon grains from the Zhongnan trachyte 2056-R10 and 2056-R14 give a weighted mean ^{206}Pb/^{238}U age of 8.91 ± 0.08 Ma ($n = 65$, MSWD = 1.5; Figure S3a), and a concordia age of 9.0 ± 0.08 Ma ($n = 29$, MSWD = 1.3; Figure S3b). U-Pb dating of zircon grains from the Zhenbei trachyte yields a weighted mean ^{206}Pb/^{238}U age of 7.80 ± 0.13 Ma and a concordia age of 8.0 ± 0.23 Ma ($n = 21$, MSWD = 3.4; Figure S3c).

5. Discussion

5.1. Fractional Crystallization and Redox Condition of the SCS Magmas

The major element compositions of the SCS seamount lavas vary widely (Figure 3). The fractionation of olivine leads to decreasing MgO, whereas clinopyroxene fractionation leads to decreasing CaO at MgO contents of <8 wt % (Figure 3d). The slight increase in V/Sc ratios with decreasing MgO below 8 wt % MgO (Figure 3f) also indicates that minor clinopyroxene fractionation likely took place, because clinopyroxene partitions V over Sc, while V is compatible in ilmenite and magnetite (C.-T. A. Lee et al., 2005). The decreasing FeO_T and TiO_2 contents in lavas with less than 4.5 wt % MgO is consistent with the crystallization of Fe-Ti oxides (e.g., ilmenite and magnetite) (Figures 3b and 3e).

Crystallization temperatures for basaltic melts were calculated using different geothermometers based on Al partitioning between coexisting olivine and Cr-spinel, and Fe/Mg partitioning between olivine and melt (Coogan et al., 2014; Danyushevsky & Plechov, 2011; Putirka, 2008). The calculated temperatures are plotted against Fo content in Figures 9a and S4b. The reported possible uncertainty, involving errors in the analysis of Al in olivine, are ±30°C for the olivine-spinel thermometry (Coogan et al., 2014), and ±20°C for the olivine-melt thermometry (Danyushevsky & Plechov, 2011). In general, the crystallization temperatures calculated using different thermometers for the same olivine agree within those uncertainties (Figures 9a and S4b). As expected, the data show progressively decreasing crystallization temperatures with decreasing olivine Fo content (Figures 9a and S4b). The calculated crystallization temperatures of the olivine phenocrysts in the SCS seamount lavas range from 1140 to 1303°C, which overlap with the range of temperatures recorded for MORB (1125–1270°C) (Coogan et al., 2014), and are considerably lower than those of mantle-plume related large-igneous providences and komatiites (Figure 9a).

Precise constraints on the variability of Earth's upper mantle redox state are critical because of their effect on our interpretation of evolution of mantle (Foley et al., 2013; Kelley & Cottrell, 2009; C.-T. A. Lee et al., 2010), and the temperature of mantle melting (Putirka et al., 2007). Because the partitioning of V between olivine and melt ($D_V^{\mathrm{Ol/melt}}$) at different redox conditions are well-studied experimentally, $D_V^{\mathrm{Ol/melt}}$ provides a reliable record of fO_2 conditions of magmas and potentially of their mantle sources (Mallmann & O'Neill, 2013).

Here we use the $D_V^{\mathrm{Ol/melt}}$ oxybarometer (Mallmann & O'Neill, 2013) to calculate the oxygen fugacity fO_2 of the SCS seamount magmas. The $D_V^{\mathrm{Ol/melt}}$ oxybarometer yields log fO_2 values ranging from ΔFMQ −0.06 to ΔFMQ +0.38 (mean 0.21) (oxygen fugacity expressed in log unit deviations from the FMQ buffer) for the Zhongnan basalts and from ΔFMQ −0.06 to ΔFMQ +0.35 (mean 0.17) for the Zhenbei basalts (Figure 9b).

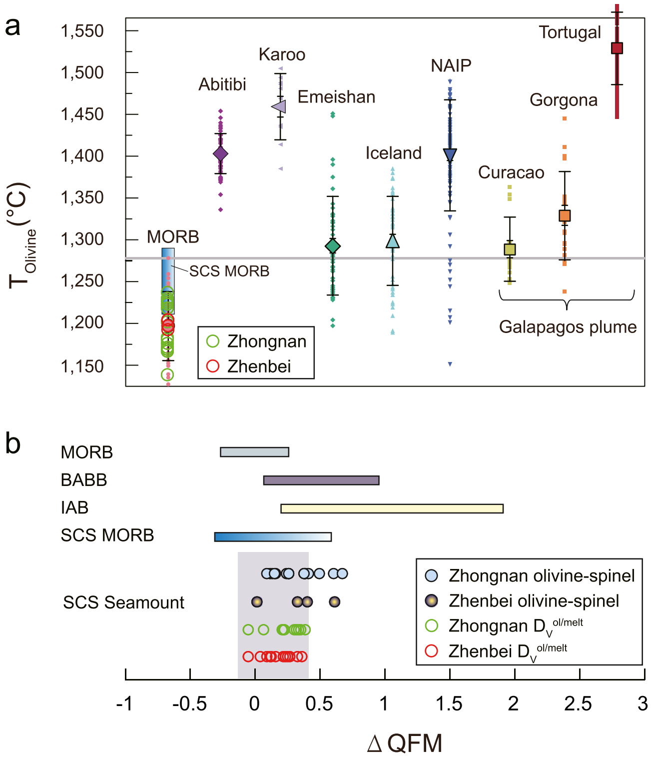

Figure 9. (a) Al-in-olivine crystallization temperatures for the South China Sea (SCS) seamount lavas in comparison to LIPs, komatiites, and other normal mid-ocean ridge basalt (MORB). Al-in-olivine crystallization temperatures for Iceland, Abitibi, Karoo, Emeishan, North Atlantic igneous province, Curacao, Gorgona, and the Tortugal terrane from Trela et al. (2017), and SCS spreading stage MORB from F. Yang et al. (2019). Al-in-olivine thermometer (Coogan et al., 2014) uses the composition of the spinel inclusions and their host olivines. Al-in-olivine thermometer is advantageous due to the slow diffusion of Al and Cr and its independence from crystallization pressure, oxygen fugacity and source lithology (Coogan et al., 2014). (b) Redox conditions (expressed as ΔFMQ) estimated for the SCS seamount magmas compared to those inferred for the SCS spreading stage MORB (F. Yang et al., 2019), MORB, BABB, and IAB (Kelley & Cottrell, 2009). Log fO_2 ΔFMQ for basalts from the SCS seamounts, Zhongnan and Zhenbei, using two different methods: $D_V^{Ol/melt}$ oxybarometer based on experimental V partitioning between olivine and melt (melt inclusion) with an uncertainty of ±0.25 log10 units fO_2 (Mallmann & O'Neil, 2013) and the spinel-olivine pairs oxybarometer (Ballhaus et al., 1991).

These values are similar to those of MORB (ΔFMQ ± 0.25; [Cottrell & Kelley, 2011]), but much more reduced compared to those typically reported for some island arc basalts (IAB; ΔFMQ +0.2–+1.8) (Kelley & Cottrell, 2009) (Figure 9b). Additionally, the spinel-olivine pair oxybarometer (Ballhaus et al., 1991) gives log fO_2 values ranging from ΔFMQ +0.10 to ΔFMQ +0.68 (mean 0.33) for the Zhongnan basalts, and from ΔFMQ +0.02 to ΔFMQ +0.62 (mean 0.34) for the Zhenbei basalts (Figure 9b), which agree with the estimates from the $D_V^{Ol/melt}$ oxybarometer. Overall, the closely comparable redox conditions inferred from different oxybarometers (Figure 9b) gives us confidence that the calculated values are reliable.

5.2. Origin of Mantle Source Components in the Late Cenozoic Lavas

The SCS seamount and SE Asia lavas have a large range in isotopic compositions (Figure 5). It is critical to determine if this isotopic variability reflects a heterogeneous source, or whether processes such as alteration or crustal contamination during magma ascent and emplacement has modified the isotopic signal. Seawater alteration might alter Sr and Mo isotopes, but do not affect Nd isotopes of oceanic lavas (Freymuth et al., 2015; Menuge et al., 1989) (Figure 5). Given the strong correlations between Sr and Mo isotope, and Nd isotope (Figure 5), the effect of seawater alteration on the Sr and Mo isotopes in our samples is most probably minimal, if any. Moreover, seawater alteration would introduce isotopically heavy, seawater-derived Mo into the uppermost oceanic crust (Freymuth et al., 2015). Thus, the relatively light Mo isotopes of the SCS lava samples are not consistent with seawater alteration and the Sr-Nd-Mo isotope compositions of the lavas are primary features.

It is noteworthy that the isotopes of most lavas do not appear to be significantly affected by crustal assimilation, as suggested by $^{143}Nd/^{144}Nd$, $^{206}Pb/^{204}Pb$, $^{187}Os/^{188}Os$, and $\delta^{98/95}Mo$ in the basalts being mostly independent of the MgO, SiO_2, Os, or Mo content in these lavas (Figure S5). Additionally, coring and seismic data have revealed the lithosphere beneath the SCS to be typical oceanic nature, and MORB-like isotopic compositions are common (low $^{87}Sr/^{86}Sr$ and high $^{143}Nd/^{144}Nd$) (G.-L. Zhang, Luo, et al., 2018; L. Zhang, Ren, et al., 2018) (Figures 5 and S5). Thus, contamination of mantle-derived melts with high MgO by oceanic lithospheric materials during magma ascent cannot account for the relatively low $^{143}Nd/^{144}Nd$ ratios of some SCS seamount lavas with low MgO (Figure S5). However, four lavas (two lavas from Hainan island and two relatively evolved trachyte 2056-R14 and R22 from Zhongnan seamount) with much more radiogenic Os isotope but low Os and MgO contents makes it likely that its Os-isotope composition reflects minor assimilation of radiogenic crust or sediments (Day, 2013) (Figure S5).

The late Cenozoic lavas from the SCS seamounts and SE Asia have overlapping isotopic compositions, which suggests that they may share common mantle sources (Figure 5a). The isotope systematics broadly define linear arrays in multi-isotope plots, consistent with mixing between a (DMM, and an EM2-like component (An et al., 2017; N. Hoang et al., 1996; T. H. A. Hoang et al., 2018; Yan et al., 2018; Zou & Fan, 2010) (Figure 5). The covariations of $\delta^{98/95}Mo$ with Sr-Nd isotopes also trace the mixing process of these two main components in the mantle. As shown in Figure 5, the SCS seamount lavas with high $^{87}Sr/^{86}Sr$ and low $^{143}Nd/^{144}Nd$ typically show low $\delta^{98/95}Mo$, indicating that at least an enriched component in the mantle source has low $\delta^{98/95}Mo$ value, while the depleted end-member shows a normal ambient mantle-like $\delta^{98/95}Mo$ value (Bezard et al., 2016; Liang et al., 2017).

Among the SCS seamount lavas, the Jiaolong seamount basalts have the most depleted Sr-Nd isotopic compositions (Figures 4 and 5a) and have the lowest trace element concentrations with typical MORB-like trace element signatures (Figure 4). The trace element (low La/Sm and Sm/Yb) and Sr-Nd isotopes (depleted Sr-Nd isotopes) of the Jiaolong seamount basalts are similar to those of the SCS spreading stage MORBs (G.-L. Zhang, Luo, et al., 2018; L. Zhang, Ren, et al., 2018), also supporting the need for a mantle endmember found in the lavas likely sampled from the asthenospheric mantle (Figures 4 and 5). Thus, the Jiaolong seamount basalts can be regarded as representing the depleted end-member, likely to be produced by partial melting of the SCS asthenosphere under a relatively thin lithosphere.

Lithospheric peridotite xenoliths entrapped by Cenozoic basalts from SE China differ significantly from the mixing line between the enriched and depleted mantle end-member in the asthenosphere (Tatsumoto et al., 1992; Xu et al., 2003) and do not support late Cenozoic lavas being directly generated from the lithospheric mantle. Additionally, the wide ranges in Os content and $^{187}Os/^{188}Os$ in late Cenozoic lavas in the SCS and surrounding area are attributed mainly to mantle source heterogeneity (Figure 5). The correlation between $^{187}Os/^{188}Os$ and $^{143}Nd/^{144}Nd$ of late Cenozoic lavas in the SCS and surrounding area indicate a high $^{187}Os/^{188}Os$ signature in the EM component (Figure 5). The SCLM beneath SE China represented by mantle peridotite xenoliths largely has relatively low $^{187}Os/^{188}Os$ (C.-Z. Liu et al., 2017), and thus makes it unlikely that the SCLM is the origin of the EM signature (Figure 5), although small degrees of melting of metasomatic veins in the SCLM observed in some locations may produce radiogenic Os signatures (as well as the enriched Sr and Nd isotope signatures).

Alternatively, the origin of the enriched composition of the late Cenozoic volcanism could be derived from an influx of Indian MORB-mantle as a result of the northern movement of the Australian Plate (Hickey-Vargas et al., 1995). Most MORBs have a slightly sub-chondritic Mo isotope composition ($\delta^{98}/^{95}Mo$ ranging from −0.24 to 0.16‰) (Bezard et al., 2016; Liang et al., 2017). Thus, the influx of Indian MORB into mantle source cannot explain the significantly light Mo isotope of some SCS seamount lavas (Figure 5). As shown in Figure S7, the array for late Cenozoic lavas is different from the Indian MORB, requiring a distinct end-member with "high $^{206}Pb/^{204}Pb$ and $^{87}Sr/^{86}Sr$, and low $^{143}Nd/^{144}Nd$," suggesting that an influx of Indian MORB mantle domain cannot account for the origin of mantle source heterogeneity of SCS marginal basin lavas.

Previous studies (Jackson et al., 2007; Willbold & Stracke, 2010; Workman et al., 2008) suggest that recycled continent-derived sediment or upper continental crust are required to explain enriched $^{87}Sr/^{86}Sr$ and $^{143}Nd/^{144}Nd$ in EM2 lavas. The correlations of $\delta^{98/95}Mo$ with $^{87}Sr/^{86}Sr$ and $^{143}Nd/^{144}Nd$ in Figure 5 indicate that the enriched component with a very light Mo isotope signature is required to explain the variation in $\delta^{98/95}Mo$ observed in these lavas. Subduction-modified (dehydrated) recycled oceanic crust and sediment may have a very light Mo isotope composition (Freymuth et al., 2015; Gaschnig et al., 2017; König et al., 2016). It is reasonable that subduction-modified recycled oceanic crust and sediment explain the low $\delta^{98/95}Mo$ signature of some SCS seamount lavas (Figure 5). Additionally, recycled oceanic crust and sediments involved in the mantle source can explain the large variation in Ba/Th and Nb/U (Figure 4d), and relatively radiogenic $^{187}Os/^{188}Os$ observed in late Cenozoic lavas (Figure 5d). Furthermore, our isotope modeling results (Figures 5 and S7) show that the source of the late Cenozoic lavas is a mixture of predominantly ambient DMM with some dehydrated recycled Mesozoic Pacific oceanic crust and sediments.

While degassing is partly responsible for these variations, there are high water concentrations that translate into high H_2O/Ce (e.g., 242–282 for the SCS volcanic glasses, this study) observed in the late Cenozoic lavas in SE China (Figure S1). H_2O/Ce (242–282) in the SCS seamount volcanic glasses (Figure 6b) are much higher than those of the lower continental crust granulites in SE China (15–28) (X. Z. Yang et al., 2008). Alteration by seawater and during subduction would modify volatile and fluid-mobile element contents (e.g., H_2O and Ba) of recycled crustal materials (Dixon et al., 2002; Kelley et al., 2005; S.-C. Liu et al., 2016). The dehydrated recycled oceanic basalts generally have low H_2O/Ce and Ba/Th ratios, while recycled altered oceanic crust and sediments can carry more water into the mantle, and have high H_2O/Ce (up to 1,200) and Ba/Th (Dixon et al., 2002; Plank & Langmuir, 1998). Thus, contamination of the upper mantle by recycled oceanic crust and sediments can explain the volatile and isotopic signature of the SCS seamount lavas. Similarly, late Cenozoic lavas in SCS surrounding areas (e.g., Zhenjiang and Hainan basalts in South China) are characterized by a large variation in H_2O/Ce (50–319 for the Hainan basalts and 100–430 for the Zhengjiang basalts; Gu et al., 2019; S.-C. Liu et al., 2016) (Figure 6), which is also consistent with incorporation of recycled oceanic materials with heterogeneous volatile contents.

5.3. Record of the Mineralogy of the Mantle Sources

Olivine is commonly the earliest silicate mineral to crystallize from mantle-derived melts. Minor and trace elements (e.g., Ca, Cr, Mn, Ni, Co, Al, and Zn) in olivine in mafic rocks have the potential to record information about the mineralogy of the mantle source that melted to produce those magmas (De Hoog et al., 2010; Foley et al., 2013; Gazel et al., 2018; Herzberg, 2011; Kamenetsky et al., 2012; Matzen, Wood, et al., 2017; Sobolev et al., 2007; Trela et al., 2017).

Olivines from the SCS seamount lavas have Ni contents that are comparable to those derived from peridotite melts (e.g., MORBs) at a given Fo value, and significantly lower than those from the Koolau basalts, Hawaii, for which large volumes of pyroxenite have been proposed in the source (Sobolev et al., 2007) (Figure 7). In addition, it has been suggested that liquids with low Mn and Ca contents observed result from partial melting of a dominantly pyroxenite source due to Mn and Ca being more compatible in pyroxene relative to olivine (Herzberg, 2011; Sobolev et al., 2007). The high Ca and Mn values of the SCS seamount olivines are similar to those for olivine in equilibrium with dominantly peridotite-derived melts (Sobolev et al., 2007) (Figures 7b and 7c). The SCS seamount olivines are more consistent with a dominantly peridotite source, with lower Fe/Mn, as well as Ni/(Mg/Fe)/100, overlapping with MORB olivines (Figures 7e and 7f). A dominantly peridotite source for the SCS seamount basalts is also supported by other first-row transition element ratios (e.g., relatively constant Zn/Fe and Zn/Mn) in the olivine phenocrysts (Le Roux et al., 2011) (Figures S6e and S6f). Therefore, the olivine phenocrysts indicate that peridotite was the main source lithology sampled by the SCS seamount lavas.

In contrast, the olivine phenocrysts in basalts from SE Asia have higher Ni contents, with an apparent gap occurring between these olivines and those from the SCS seamount basalts and MORBs (Figure 7a). Two main processes may result in the clear difference in Ni contents of olivine phenocrysts from the SCS seamount basalts, and those in basalts from SE Asia: (a) a different mantle source mineralogy (Herzberg, 2011; Sobolev et al., 2007; X. C. Wang et al., 2012), and (b) differences in the pressure at which partial melts segregate from the mantle source (Howarth & Harris, 2017; Matzen, Baker, et al., 2017; Niu et al., 2011).

An olivine-poor, pyroxenitic mantle source would partition more Ni into the liquid phase than peridotite source during partial melting owing to the lower bulk partition coefficient for Ni (Herzberg, 2011; Sobolev et al., 2007). Ni and Mn contents in olivines from late Cenozoic basalts from SE Asia and SCS seamount correlate with their lithospheric thickness (Figure 8). At a fixed mantle temperature, pyroxenite commonly begins to melt at higher pressures than peridotite (Herzberg, 2011; Sobolev et al., 2007); thus, in the SE Asia, where the lithosphere is thick, the mean partial melting depth is higher, and the final melts produced would be expected to include a larger proportion of pyroxenite-derived liquids. A similar feature is also observed for the natural data set: olivines that erupt on thin lithosphere tend to have low Ni and high Mn contents, while olivines erupted on thicker lithosphere largely have higher Ni and lower Mn contents (e.g., MORBs) (Matzen, Wood, et al., 2017; Sobolev et al., 2007) (Figure 8). Alternatively, the observed variations in Ni and Mn is attributed to pressure-related variations of the partition coefficient of nickel in olivine (Matzen, Baker, et al., 2017; Niu et al., 2011). The range of $(NiO/MnO)_{Fo89}$ ratios for the SCS seamount olivines analyzed in this study are similar to the results from experiments by Matzen, Baker, et al. (2017) at 1 GPa (10 kbar), as well as those for olivine where the lithosphere is thin, such as Iceland and MORB, compiled by Matzen, Wood, et al. (2017) (Figures 8a and 8b). This suggests that the Ni and Mn contents of the SCS seamount olivines are consistent with partial melts of peridotites segregating at various pressures corresponding to the lithosphere-asthenosphere boundary (LAB). The higher Ni contents in the SE Asia olivines relative to the olivines from the SCS seamounts can be largely explained by differences in mantle melting depth (Figure 8b), with the SE Asia olivines coming from deeper. Furthermore, the depths of mantle melting (Figure 8b) independently predicted by the correlation between Mn-Ni contents of olivine phenocrysts observed and the model results of Matzen, Baker, et al. (2017) agree, within uncertainty, with well constrained geophysical data that indicate that the LAB beneath the SCS and SE Asia is at a depth of 40 and 60–75 km, respectively (Wu et al., 2004; T. Yang et al., 2015). Similar lithological characteristics for the source of these basalts is also supported by the similarity in whole-rock chemical and isotopic compositions between the

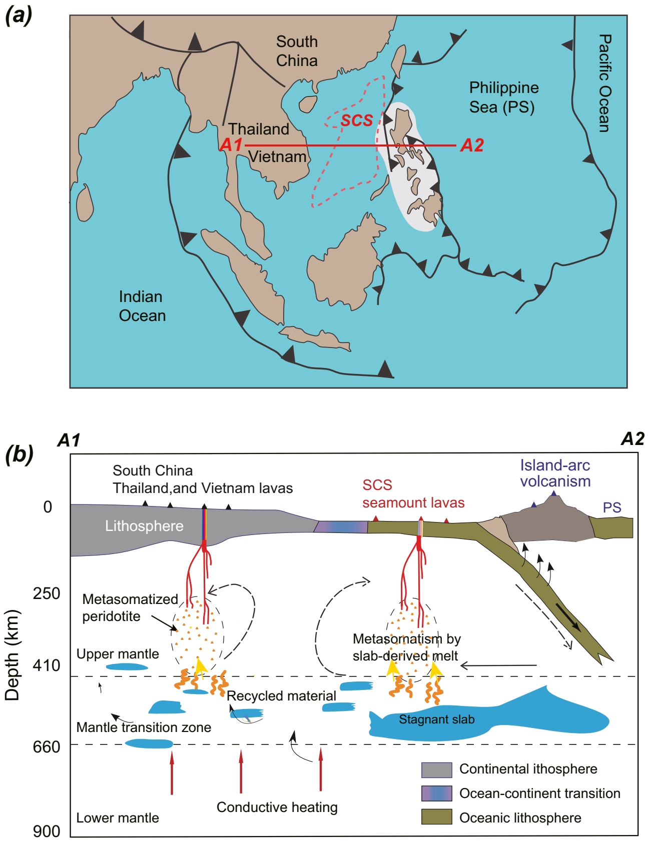

Figure 10. (a) Map of the South China Sea (SCS) and adjacent regions. (b) Schematic cross section (line A1–A2 in (a)) illustrating magmatism caused by decompression-induced partial melting of mantle upwelling from the mantle transition zone to the shallow asthenosphere during the Cenozoic in Southeast Asia.

SE and the SCS seamount basalts (Figures 3, 4 and 5a). Thus, although a recycled pyroxenitic component cannot be ruled out in the mantle source regions of basalts from the SCS seamount and SE Asia, major and minor elements (including the observed Ni and Mn contents of olivines) can be simply explained by partial melting of a dominantly peridotitic source.

5.4. A Model for the Generation of Late Cenozoic Magmatism

The lack of age progression and discrete erupted volumes of late Cenozoic magmatism in SE Asia argue against a deeply rooted mantle plume as the source of these intraplate volcanoes. The low crystallization temperatures of the SCS seamount lavas (Figure 9) are also inconsistent with a hot-plume anchored in the deep mantle. Finally, the ^{3}He/^{4}He of the SCS seamount basalts are among the range reported for MORB away from hotspot influence (Figures 6c and 6d). Therefore, it is necessary to propose an alternative model to explain the origin of late Cenozoic magmatism along SE Asia.

Geophysical studies have identified stagnant oceanic slabs in the mantle transition zone (MTZ) beneath SE Asia (Huang et al., 2015; C. Li et al., 2008). Numerical modeling suggests that slab stagnation and retreat have the potential to trigger mantle upwelling around the MTZ (J. Yang & Faccenda, 2020). Here, we propose that the stagnant slab triggered instabilities in the MTZ that resulted in discrete but widespread upwellings, consistent with the small-scale footprint of intraplate volcanoes in the SCS and SE Asia (Figure 10). In this case, according to Thomson et al. (2016), the thermal gradient of the subducted slab, whether hot or cold, would intersect the solidi of carbonated peridotite/eclogite in the MTZ. Carbonated fluids/melts from subducted ocean crust and marine sediments stored in the transition zone could have metasomatized the overlying mantle. Carbonated silicate melts found in the post-spreading stage provide direct evidence for CO$_2$ in the mantle beneath the SCS (G.-L. Zhang et al., 2017). Models that suggest upwelling induced by stagnant slabs have also been proposed to explain other intraplate volcanic regions in the Tethyan tectonic belt (e.g., Mediterranean and Turkish-Iranian Plateau) characterized by subduction of the Tethys Ocean (Lustrino & Wilson, 2007; Soltanmohammadi et al., 2018), the extreme HIMU lavas from Bermuda (Mazza et al., 2019), Australia's east coast volcanoes (Mather et al., 2020), and Eastern China associated with the long-term subduction of the Pacific slab (J. Yang & Faccenda, 2020). Notably, the lavas erupted in different volcanic regions sample distinct mantle reservoirs from the MTZ. For example, Cenozoic lavas in northeast China sampled a dominantly EM1 component (X.-J. Wang et al., 2017), while the volcanic fields of east Australia-Zealandia have sampled two distinct mantle reservoirs from the MTZ: HIMU in the south and EM1/EM2 in the north (Mather et al., 2020).

An important question is how the recycled oceanic crust and sediment signature is transferred to the mantle source of late Cenozoic lavas. As mentioned above, the geochemical compositions of late Cenozoic lavas are readily interpreted by mixing a depleted mantle source with small amounts of recycled Mesozoic Pacific oceanic and sediment, reflecting a more recent influx of oceanic lithosphere into the MTZ. Thus, it is possible that the late Cenozoic lavas sample an EM reservoir near the MTZ consistent with past subduction (possibly related to Paleo-Pacific plate subduction), and the magmas acquired the enriched signature from recycled materials at relatively shallow levels in the upper mantle.

We note that the compositions (e.g., low trace element contents, La/Sm and Sm/Yb, and depleted Sr and Nd isotope) of the Jiaolong seamount tholeiites resemble the SCS spreading-stage MORBs (Figures 4 and 5a). The lavas from other seamounts (Shixingbei, Zhongnan, and Zhenbei) show trace element patterns that are more enriched than the SCS spreading basalts (high trace element contents, La/Sm and Sm/Yb, Figure 4), and have higher ^{87}Sr/^{86}Sr, and lower ^{143}Nd/^{144}Nd than the SCS spreading-stage MORBs (Figures 4 and 5a).

Shallow processes such as variations in lithospheric thickness that together with mantle source heterogeneity (a mixture of different components with different solidus temperatures), lead to compositionally distinct melting trends observed in this study. A large degree of partial melting under a thin lithosphere produces normal MORB-like melts represented by some Jiaolong seamount and spreading ridge lavas. In contrast, under thick lithosphere, chemically enriched and more fusible mantle components melt preferentially at deeper depths, thereby lowering the degree of melting of surrounding refractory mantle peridotite (Sleep, 1984). In that case, these melts record geochemically enriched and more fusible mantle components with higher alkalies and volatile contents. Consequently, the higher degrees of melting and magma mixing during the spreading stage have erased much of the heterogeneity in the upper mantle beneath the SCS.

6. Conclusions

This study presents zircon U-Pb ages, olivine, spinel and melt inclusion compositions, as well as whole-rock chemical and Sr-Nd-Mo-Os isotopic compositions of lavas from the SCS Zhongnan and Zhenbei seamounts, and glass compositions and whole-rock chemical and Sr-Nd isotopic compositions of lavas from the SCS Jiaolong and Shixibei seamounts.

1. Zircon dating results show that Zhongnan and Zhenbei seamounts formed at 9.0 and 7.80 Ma, respectively.
2. Isotope data, together with previously published results of late Cenozoic lavas from SE Asia, can be explained by mixing between an EM2 mantle and a DMM component. The EM2 signature was inherited from recycled young oceanic crust and sediments.
3. Olivine phenocryst compositions indicate that late Cenozoic melts were derived from an olivine-dominated (peridotitic) mantle source.
4. Combined with geophysical data and tectonic evolution, late Cenozoic magmatism is not related to a deep mantle plume but is more consistent with widespread upwelling from the MTZ triggered by a thermal/physical instability due to the occurrence of a stagnant slab.
5. Our study provides new insights into the role of deep recycling of subducted oceanic crust stagnant within the MTZ in generating mantle heterogeneities.

Data Availability Statement

The data in this paper are available in Zenodo Data (http://doi.org/10.5281/zenodo.5089069) or Supporting Information.

Acknowledgments
This study was supported by the National Key Research and Development Project of China (2020YFA0714800) and the National Natural Science Foundation of China (41902044 and 91428207). The authors are grateful to the Editor Janne Blichert-Toft, Alessio Sanfilippo, and two anonymous reviewers for providing lots of helpful suggestions and comments. The authors thank Tamara Baumberger, Wanfeng Zhang, Qing Yang, Lingmin Zhang, and Zhibing Wang for assistance in the sample analysis. Discussions with Kaj Hoernle, Yigang Xu, David Peate, and Zhongyuan Ren are appreciated.

References

An, A. R., Choi, S. H., Yu, Y., & Lee, D.-C. (2017). Petrogenesis of Late Cenozoic basaltic rocks from southern Vietnam. *Lithos*, *272–273*, 192–204. https://doi.org/10.1016/j.lithos.2016.12.008

Andersen, T. (2002). Correction of common lead in U–Pb analyses that do not report 204Pb. *Chemical Geology*, *192*(1), 59–79. https://doi.org/10.1016/S0009-2541(02)00195-X

Anderson, D. L. (2001). Top-down tectonics? *Science*, *293*(5537), 2016–2018. https://doi.org/10.1126/science.1065448

Ballhaus, C., Berry, R. F., & Green, D. H. (1991). High pressure experimental calibration of the olivine-orthopyroxene-spinel oxygen geobarometer: Implications for the oxidation state of the upper mantle. *Contributions to Mineralogy and Petrology*, *107*(1), 27–40. https://doi.org/10.1007/BF00311183

Bezard, R., Fischer-Gödde, M., Hamelin, C., Brennecka, G. A., & Kleine, T. (2016). The effects of magmatic processes and crustal recycling on the molybdenum stable isotopic composition of mid-ocean ridge basalts. *Earth and Planetary Science Letters*, *453*, 171–181. https://doi.org/10.1016/j.epsl.2016.07.056

Blichert-Toft, J., Frey, F. A., & Albarede, F. (1999). Hf isotope evidence for pelagic sediments in the source of Hawaiian basalts. *Science*, *285*(5429), 879–882. https://doi.org/10.1126/science.285.5429.879

Brandon, A. D., & Walker, R. J. (2005). The debate over core–mantle interaction. *Earth and Planetary Science Letters*, *232*(3), 211–225. https://doi.org/10.1016/j.epsl.2005.01.034

Chauvel, C., Hofmann, A. W., & Philippe, V. (1992). HIMU-EM, the French Polynesian connection. *Earth and Planetary Science Letters*, *110*, 99–119. https://doi.org/10.1016/0012-821X(92)90042-T

Chauvel, C., Lewin, E., Carpentier, M., Arndt, N. T., & Marini, J. C. (2008). Role of recycled oceanic basalt and sediment in generating the Hf–Nd mantle array. *Nature Geoscience*, *1*, 64–67. https://doi.org/10.1038/ngeo.2007.51

Class, C., & Goldstein, S. L. (2005). Evolution of helium isotopes in the Earth's mantle. *Nature*, *436*(7054), 1107–1112. https://doi.org/10.1038/nature03930

Coogan, L. A., Saunders, A. D., & Wilson, R. N. (2014). Aluminum-in-olivine thermometry of primitive basalts: Evidence of an anomalously hot mantle source for large igneous provinces. *Chemical Geology*, *368*, 1–10. https://doi.org/10.1016/j.chemgeo.2014.01.004

Cottrell, E., & Kelley, K. A. (2011). The oxidation state of Fe in MORB glasses and the oxygen fugacity of the upper mantle. *Earth and Planetary Science Letters*, *305*(3), 270–282. https://doi.org/10.1016/j.epsl.2011.03.014

Dale, C. W., Luguet, A., Macpherson, C. G., Pearson, D. G., & Hickey-Vargas, R. (2008). Extreme platinum-group element fractionation and variable Os isotope compositions in Philippine Sea Plate basalts: Tracing mantle source heterogeneity. *Chemical Geology*, *248*(3), 213–238. https://doi.org/10.1016/j.chemgeo.2007.11.007

Dale, C. W., Pearson, D. G., Starkey, N. A., Stuart, F. M., Ellam, R. M., Larsen, L. M., et al. (2009). Osmium isotopes in Baffin Island and West Greenland picrites: Implications for the ^{187}Os/^{188}Os composition of the convecting mantle and the nature of high ^{3}He/^{4}He mantle. *Earth and Planetary Science Letters*, *278*(3), 267–277. https://doi.org/10.1016/j.epsl.2008.12.014

Danyushevsky, L. V., & Plechov, P. (2011). Petrolog3: Integrated software for modeling crystallization processes. *Geochemistry, Geophysics, Geosystems*, *12*, Q07021. https://doi.org/10.1029/2011gc003516

Day, J. M. D. (2013). Hotspot volcanism and highly siderophile elements. *Chemical Geology*, *341*, 50–74. https://doi.org/10.1016/j.chemgeo.2012.12.010

Day, J. M. D., Hilton, D. R., Pearson, D. G., Macpherson, C. G., Kjarsgaard, B. A., & Janney, P. E. (2005). Absence of a high time-integrated ^{3}He/(U+Th) source in the mantle beneath continents. *Geology*, *33*(9), 733–736. https://doi.org/10.1130/g21625.1

De Hoog, J. C. M., Gall, L., & Cornell, D. H. (2010). Trace-element geochemistry of mantle olivine and application to mantle petrogenesis and geothermobarometry. *Chemical Geology*, *270*(1), 196–215. https://doi.org/10.1016/j.chemgeo.2009.11.017

Dixon, J. E., Dixon, T. H., Bell, D. R., & Malservisi, R. (2004). Lateral variation in upper mantle viscosity: Role of water. *Earth and Planetary Science Letters*, *222*(2), 451–467. https://doi.org/10.1016/j.epsl.2004.03.022

Dixon, J. E., Leist, L., Langmuir, C., & Schilling, J.-G. (2002). Recycled dehydrated lithosphere observed in plume-influenced mid-ocean-ridge basalt. *Nature*, *420*(6914), 385–389. https://doi.org/10.1038/nature01215

Fan, J.-J., Li, J., Wang, Q., Zhang, L., Zhang, J., Zeng, X.-L., et al. (2020). High-precision molybdenum isotope analysis of low-Mo igneous rock samples by MC–ICP–MS. *Chemical Geology*, *545*, 119648. https://doi.org/10.1016/j.chemgeo.2020.119648

Foley, S. F., Prelevic, D., Rehfeldt, T., & Jacob, D. E. (2013). Minor and trace elements in olivines as probes into early igneous and mantle melting processes. *Earth and Planetary Science Letters*, *363*, 181–191. https://doi.org/10.1016/j.epsl.2012.11.025

Freymuth, H., Vils, F., Willbold, M., Taylor, R. N., & Elliott, T. (2015). Molybdenum mobility and isotopic fractionation during subduction at the Mariana arc. *Earth and Planetary Science Letters*, *432*, 176–186. https://doi.org/10.1016/j.epsl.2015.10.006

Gannoun, A., Burton, K. W., Parkinson, I. J., Alard, O., Schiano, P., & Thomas, L. E. (2007). The scale and origin of the osmium isotope variations in mid-ocean ridge basalts. *Earth and Planetary Science Letters*, *259*(3), 541–556. https://doi.org/10.1016/j.epsl.2007.05.014

Gaschnig, R. M., Reinhard, C. T., Planavsky, N. J., Wang, X., Asael, D., & Chauvel, C. (2017). The molybdenum isotope system as a tracer of slab input in subduction zones: An example from Martinique, Lesser Antilles arc. *Geochemistry, Geophysics, Geosystems*, *18*(12), 4674–4689. https://doi.org/10.1002/2017gc007085

Gazel, E., Trela, J., Bizimis, M., Sobolev, A., Batanova, V., Class, C., & Jicha, B. (2018). Long-lived source heterogeneities in the Galapagos mantle plume. *Geochemistry, Geophysics, Geosystems*, *19*(8), 2764–2779. https://doi.org/10.1029/2017GC007338

Greber, N. D., Siebert, C., Nägler, T. F., & Pettke, T. (2012). $\delta^{98/95}$Mo values and molybdenum concentration data for NIST SRM 610, 612 and 3134: Towards a common protocol for reporting Mo data. *Geostandards and Geoanalytical Research*, *36*(3), 291–300. https://doi.org/10.1111/j.1751-908X.2012.00160.x

Gu, X.-Y., Wang, P.-Y., Kuritani, T., Hanski, E., Xia, Q.-K., & Wang, Q.-Y. (2019). Low water content in the mantle source of the Hainan plume as a factor inhibiting the formation of a large igneous province. *Earth and Planetary Science Letters*, *515*, 221–230. https://doi.org/10.1016/j.epsl.2019.03.034

Hauff, F., Hoernle, K., & Schmidt, A. (2003). Sr-Nd-Pb composition of Mesozoic Pacific oceanic crust (Site 1149 and 801, ODP Leg 185): Implications for alteration of ocean crust and the input into the Izu-Bonin-Mariana subduction system. *Geochemistry, Geophysics, Geosystems*, *4*(8). https://doi.org/10.1029/2002gc000421

Hayes, G. P., Moore, G. L., Portner, D. E., Hearne, M., Flamme, H., Furtney, M., & Smoczyk, G. M. (2018). Slab2, a comprehensive subduction zone geometry model. *Science*, *362*(6410), 58–61. https://doi.org/10.1126/science.aat4723

Herzberg, C. (2011). Identification of source lithology in the Hawaiian and Canary Islands: Implications for origins. *Journal of Petrology*, *52*(1), 113–146. https://doi.org/10.1093/petrology/egq075

Herzberg, C., Cabral, R. A., Jackson, M. G., Vidito, C., Day, J. M. D., & Hauri, E. H. (2014). Phantom Archean crust in Mangaia hotspot lavas and the meaning of heterogeneous mantle. *Earth and Planetary Science Letters*, *396*, 97–106. https://doi.org/10.1016/j.epsl.2014.03.065

Hickey-Vargas, R., Hergt, J., & Spadea, P. (1995). The Indian Ocean-type isotopic signature in western Pacific marginal basins: Origin and significance. In B. Taylor & J. Natland (Eds.), *Active margins and marginal basins of the Western Pacific* (Geophysical Monograph Series, Vol. 88, pp. 175–197). American Geophysical Union. https://doi.org/10.1029/GM088p0175

Ho, K.-S., Chen, J.-C., Lo, C.-H., & Zhao, H.-L. (2003). ^{40}Ar–^{39}Ar dating and geochemical characteristics of late Cenozoic basaltic rocks from the Zhejiang–Fujian region, SE China: Eruption ages, magma evolution and petrogenesis. *Chemical Geology*, *197*(1–4), 287–318. https://doi.org/10.1016/S0009-2541(02)00399-6

Hoang, N., Flower, M. F. J., & Carlson, R. W. (1996). Major, trace element, and isotopic compositions of Vietnamese basalts: Interaction of hydrous EM1-rich asthenosphere with thinned Eurasian lithosphere. *Geochimica et Cosmochimica Acta*, *60*(22), 4329–4351. https://doi.org/10.1016/S0016-7037(96)00247-5

Hoang, T. H. A., Choi, S. H., Yu, Y., Pham, T. H., Nguyen, K. H., & Ryu, J.-S. (2018). Geochemical constraints on the spatial distribution of recycled oceanic crust in the mantle source of late Cenozoic basalts, Vietnam. *Lithos*, *296–299*, 382–395. https://doi.org/10.1016/j.lithos.2017.11.020

Hofmann, A. W. (1988). Chemical differentiation of the Earth: The relationship between mantle, continental crust, and oceanic crust. *Earth and Planetary Science Letters*, *90*(3), 297–314. https://doi.org/10.1016/0012-821X(88)90132-X

Hofmann, A. W. (1997). Mantle geochemistry: The message from oceanic volcanism. *Nature*, *385*(6613), 219–229. https://doi.org/10.1038/385219a0

Howarth, G. H., & Harris, C. (2017). Discriminating between pyroxenite and peridotite sources for continental flood basalts (CFB) in southern Africa using olivine chemistry. *Earth and Planetary Science Letters*, *475*, 143–151. https://doi.org/10.1016/j.epsl.2017.07.043

Huang, Z., Zhao, D., & Wang, L. (2015). P wave tomography and anisotropy beneath Southeast Asia: Insight into mantle dynamics. *Journal of Geophysical Research: Solid Earth*, *120*, 5154–5174. https://doi.org/10.1002/2015JB012098

Humayun, M., Qin, L., & Norman, M. D. (2004). Geochemical evidence for excess iron in the mantle beneath Hawaii. *Science*, *306*(5693), 91–94. https://doi.org/10.1126/science.1101050

Ishikawa, A., Senda, R., Suzuki, K., Dale, C., & Meisel, T. (2014). Re-evaluating digestion methods for highly siderophile element and ^{187}Os isotope analysis: Evidence from geological reference materials. *Chemical Geology*, *384*, 27–46. https://doi.org/10.1016/j.chemgeo.2014.06.013

Isnard, H., Brennetot, R., Caussignac, C., Caussignac, N., & Chartier, F. (2005). Investigations for determination of Gd and Sm isotopic compositions in spent nuclear fuels samples by MC ICPMS. *International Journal of Mass Spectrometry*, *246*, 66–73. https://doi.org/10.1016/j.ijms.2005.08.008

Jackson, M. G., Becker, T. W., & Konter, J. G. (2018). Evidence for a deep mantle source for EM and HIMU domains from integrated geochemical and geophysical constraints. *Earth and Planetary Science Letters*, *484*, 154–167. https://doi.org/10.1016/j.epsl.2017.11.052

Jackson, M. G., Hart, S. R., Koppers, A. A. P., Staudigel, H., Konter, J., Blusztajn, J., et al. (2007). The return of subducted continental crust in Samoan lavas. *Nature*, *448*, 684–687. https://doi.org/10.1038/nature06048

Kamenetsky, V. S., Chung, S. L., Kamenetsky, M. B., & Kuzmin, D. V. (2012). Picrites from the Emeishan large igneous province, SW China: A compositional continuum in primitive magmas and their respective mantle sources. *Journal of Petrology*, *53*(10), 2095–2113. https://doi.org/10.1093/petrology/egs045

Kelley, K. A., & Cottrell, E. (2009). Water and the oxidation state of subduction zone magmas. *Science*, *325*(5940), 605–607. https://doi.org/10.1126/science.1174156

Kelley, K. A., Plank, T., Farr, L., Ludden, J., & Staudigel, H. (2005). Subduction cycling of U, Th, and Pb. *Earth and Planetary Science Letters*, *234*(3–4), 369–383. https://doi.org/10.1016/j.epsl.2005.03.005

König, S., Wille, M., Voegelin, A., & Schoenberg, R. (2016). Molybdenum isotope systematics in subduction zones. *Earth and Planetary Science Letters*, *447*, 95–102. https://doi.org/10.1016/j.epsl.2016.04.033

Konter, J. G., & Becker, T. W. (2012). Shallow lithospheric contribution to mantle plumes revealed by integrating seismic and geochemical data. *Geochemistry, Geophysics, Geosystems*, *13*, Q02004. https://doi.org/10.1029/2011GC003923

Lee, C.-T. A., Leeman, W. P., Canil, D., & Li, Z.-X. A. (2005). Similar V/Sc systematics in MORB and arc basalts: Implications for the oxygen fugacities of their mantle source regions. *Journal of Petrology*, *46*(11), 2313–2336. https://doi.org/10.1093/petrology/egi056

Lee, C.-T. A., Luffi, P., Le Roux, V., Dasgupta, R., Albaréde, F., & Leeman, W. P. (2010). The redox state of arc mantle using Zn/Fe systematics. *Nature*, *468*(7324), 681–685. https://doi.org/10.1038/nature09617

Lee, C.-Y., Tsai, J. H., Ho, H. H., Yang, T. F., Chung, S.-L., & Chen, C. H. (1997). *Quantitative analysis in rock samples by an X-ray fluorescence spectrometer (I) major elements* (pp. 418–430). Program with Abstracts of 1997, Annual Meeting of Geological Society of China.

Le Roux, V., Dasgupta, R., & Lee, C. T. A. (2011). Mineralogical heterogeneities in the Earth's mantle: Constraints from Mn, Co, Ni and Zn partitioning during partial melting. *Earth and Planetary Science Letters*, *307*(3–4), 395–408. https://doi.org/10.1016/j.epsl.2011.05.014

Le Voyer, M., Hauri, E. H., Cottrell, E., Kelley, K. A., Salters, V. J. M., Langmuir, C. H., et al. (2019). Carbon fluxes and primary magma CO_2 contents along the global mid-ocean ridge system. *Geochemistry, Geophysics, Geosystems*, *20*, 1387–1424. https://doi.org/10.1029/2018gc007630

Li, C., van derHilst, R. D., Engdahl, E. R., & Burdick, S. (2008). A new global model for P wave speed variations in Earth's mantle. *Geochemistry, Geophysics, Geosystems*, *9*, Q05018. https://doi.org/10.1029/2007GC001806

Li, C.-F., Xu, X., Lin, J., Sun, Z., Zhu, J., Yao, Y., et al. (2014). Ages and magnetic structures of the South China Sea constrained by deep tow magnetic surveys and IODP Expedition 349. *Geochemistry, Geophysics, Geosystems*, *15*(12), 4958–4983. https://doi.org/10.1002/2014GC005567

Li, J., Liang, X.-R., Zhong, L.-F., Wang, X.-C., Ren, Z.-Y., Sun, S.-L., et al. (2014). Measurement of the isotopic composition of molybdenum in geological samples by MC-ICP-MS using a novel chromatographic extraction technique. *Geostandards and Geoanalytical Research*, *38*(3), 345–354. https://doi.org/10.1111/j.1751-908X.2013.00279.x

Li, J., Wang, X.-C., Xu, J.-F., Xu, Y.-G., Tang, G.-J., & Wang, Q. (2015). Disequilibrium-induced initial Os isotopic heterogeneity in gram aliquots of single basaltic rock powders: Implications for dating and source tracing. *Chemical Geology*, *406*, 10–17. https://doi.org/10.1016/j.chemgeo.2015.04.010

Li, J., Zhao, P.-P., Liu, J., Wang, X.-C., Yang, A. Y., Wang, G.-Q., & Xu, J.-F. (2015). Reassessment of hydrofluoric acid desilicification in the Carius tube digestion technique for Re–Os isotopic determination in geological samples. *Geostandards and Geoanalytical Research*, *39*, 17–30. https://doi.org/10.1111/j.1751-908X.2014.00299.x

Li, J. I. E., Liang, X.-R., Xu, J.-F., Suzuki, K., & Dong, Y.-H. (2010). Simplified technique for the measurements of Re-Os isotope by multicollector inductively coupled plasma mass spectrometry (MC-ICP-MS). *Geochemical Journal*, *44*, 73–80. https://doi.org/10.2343/geochemj.1.0044

Liang, Y.-H., Halliday, A. N., Siebert, C., Fitton, J. G., Burton, K. W., Wang, K.-L., & Harvey, J. (2017). Molybdenum isotope fractionation in the mantle. *Geochimica et Cosmochimica Acta*, *199*, 91–111. https://doi.org/10.1016/j.gca.2016.11.023

Liu, C.-Z., Snow, J. E., Hellebrand, E., Brügmann, G., von der Handt, A., Büchl, A., & Hofmann, A. W. (2008). Ancient, highly heterogeneous mantle beneath Gakkel ridge, Arctic Ocean. *Nature*, *452*(7185), 311–316. https://doi.org/10.1038/nature06688

Liu, C.-Z., Zhang, C., Liu, Z.-C., Sun, J., Chu, Z.-Y., Qiu, Z.-L., & Wu, F.-Y. (2017). Formation age and metasomatism of the sub-continental lithospheric mantle beneath southeast China: Sr-Nd-Hf-Os isotopes of Mingxi mantle xenoliths. *Journal of Asian Earth Sciences*, *145*, 591–604. https://doi.org/10.1016/j.jseaes.2017.06.013

Liu, J. Q., Ren, Z. Y., Nichols, A. R. L., Song, M. S., Qian, S. P., Zhang, Y., & Zhao, P. P. (2015). Petrogenesis of Late Cenozoic basalts from North Hainan Island: Constraints from melt inclusions and their host olivines. *Geochimica et Cosmochimica Acta*, *152*, 89–121. https://doi.org/10.1016/j.gca.2014.12.023

Liu, S.-C., Xia, Q.-K., Choi, S. H., Deloule, E., Li, P., & Liu, J. (2016). Continuous supply of recycled Pacific oceanic materials in the source of Cenozoic basalts in SE China: The Zhejiang case. *Contributions to Mineralogy and Petrology*, *171*(12), 100. https://doi.org/10.1007/s00410-016-1310-4

Liu, Y., Hu, Z., Gao, S., Günther, D., Xu, J., Gao, C., & Chen, H. (2008). In situ analysis of major and trace elements of anhydrous minerals by LA-ICP-MS without applying an internal standard. *Chemical Geology*, *257*, 34–43. https://doi.org/10.1016/j.chemgeo.2008.08.004

Li, X.-H., Li, Z.-X., Wingate, M. T. D., Chung, S.-L., Liu, Y., Lin, G.-C., & Li, W.-X. (2006). Geochemistry of the 755 Ma Mundine Well dyke swarm, northwestern Australia: Part of a Neoproterozoic mantle superplume beneath Rodinia? *Precambrian Research*, *146*, 1–15. https://doi.org/10.1016/j.precamres.2005.12.007

Lupton, J., Rubin, K. H., Arculus, R., Lilley, M., Butterfield, D., Resing, J., et al. (2015). Helium isotope, C/^{3}He, and Ba-Nb-Ti signatures in the northern Lau Basin: Distinguishing arc, back-arc, and hotspot affinities. *Geochemistry, Geophysics, Geosystems*, *16*(4), 1133–1155. https://doi.org/10.1002/2014gc005625

Lustrino, M., & Wilson, M. (2007). The circum-Mediterranean anorogenic Cenozoic igneous province. *Earth-Science Reviews*, *81*(1), 1–65. https://doi.org/10.1016/j.earscirev.2006.09.002

Ma, J., Wei, G., Liu, Y., Ren, Z., Xu, Y., & Yang, Y. (2013). Precise measurement of stable neodymium isotopes of geological materials by using MC-ICP-MS. *Journal of Analytical Atomic Spectrometry*, *28*, 1926–1931. https://doi.org/10.1039/C3JA50229E

Mallmann, G., & O'Neill, H. S. C. (2013). Calibration of an empirical thermometer and oxybarometer based on the partitioning of Sc, Y and V between olivine and silicate melt. *Journal of Petrology*, *54*(5), 933–949. https://doi.org/10.1093/petrology/egt001

Mather, B. R., Müller, R. D., Seton, M., Ruttor, S., Nebel, O., & Mortimer, N. (2020). Intraplate volcanism triggered by bursts in slab flux. *Science Advances*, *6*(51), eabd0953. https://doi.org/10.1126/sciadv.abd0953

Matzen, A. K., Baker, M. B., Beckett, J. R., Wood, B. J., & Stolper, E. M. (2017). The effect of liquid composition on the partitioning of Ni between olivine and silicate melt. *Contributions to Mineralogy and Petrology*, *172*(1), 3. https://doi.org/10.1007/s00410-016-1319-8

Matzen, A. K., Wood, B. J., Baker, M. B., & Stolper, E. M. (2017). The roles of pyroxenite and peridotite in the mantle sources of oceanic basalts. *Nature Geoscience*, *10*(7), 530–535. https://doi.org/10.1038/ngeo2968

Mazza, S. E., Gazel, E., Bizimis, M., Moucha, R., Béguelin, P., Johnson, E. A., et al. (2019). Sampling the volatile-rich transition zone beneath Bermuda. *Nature*, *569*(7756), 398–403. https://doi.org/10.1038/s41586-019-1183-6

Meisel, T., Walker, R. J., Irving, A. J., & Lorand, J.-P. (2001). Osmium isotopic compositions of mantle xenoliths: A global perspective. *Geochimica et Cosmochimica Acta*, *65*(8), 1311–1323. https://doi.org/10.1016/S0016-7037(00)00566-4

Menuge, J., Pedersen., & Furnes, H. (1989). Seawater alteration of the Karmøy Ophiolite Complex, SW Norway: Nd and Sr isotopic evidence. *Norsk Geologisk Tidsskrift*, *69*, 191–200.

Mundl, A., Touboul, M., Jackson, M. G., Day, J. M. D., Kurz, M. D., Lekic, V., et al. (2017). Tungsten-182 heterogeneity in modern ocean island basalts. *Science*, *356*(6333), 66–69. https://doi.org/10.1126/science.aal4179

Nguyen, H., Flower, M. F. J., & Carlson, R. W. (1996). Major, trace element, and isotopic compositions of Vietnamese basalts: Interaction of hydrous EM1-rich asthenosphere with thinned Eurasian lithosphere. *Geochimica et Cosmochimica Acta*, *60*(22), 4329–4351.

Nier, A. (1938). The isotopic constitution of strontium, barium, bismuth, thallium and mercury. *Physical Review*, *54*, 275–278. https://doi.org/10.1103/PhysRev.54.275

Niu, Y. L., Wilson, M., Humphreys, E. R., & O'Hara, M. J. (2011). The origin of intra-plate ocean island basalts (OIB): The lid effect and its geodynamic implications. *Journal of Petrology*, *52*(7–8), 1443–1468. https://doi.org/10.1093/petrology/egr030

Pearson, D. G., Brenker, F. E., Nestola, F., McNeill, J., Nasdala, L., Hutchison, M. T., et al. (2014). Hydrous mantle transition zone indicated by ringwoodite included within diamond. *Nature*, *507*(7491), 221–224. https://doi.org/10.1038/nature13080

Peucker-Ehrenbrink, B., Hanghoj, K., Atwood, T., & Kelemen, P. B. (2012). Rhenium-osmium isotope systematics and platinum group element concentrations in oceanic crust. *Geology*, *40*(3), 199–202. https://doi.org/10.1130/G32431.1

Peucker-Ehrenbrink, B., Ravizza, G., & Hofmann, A. W. (1995). The marine ^{187}Os/^{186}Os record of the past 80 million years. *Earth and Planetary Science Letters*, *130*(1), 155–167. https://doi.org/10.1016/0012-821X(95)00003-U

Pietruszka, A. J., Norman, M. D., Garcia, M. O., Marske, J. P., & Burns, D. H. (2013). Chemical heterogeneity in the Hawaiian mantle plume from the alteration and dehydration of recycled oceanic crust. *Earth and Planetary Science Letters*, *361*, 298–309. https://doi.org/10.1016/j.epsl.2012.10.030

Plank, T., & Langmuir, C. H. (1998). The chemical composition of subducting sediment and its consequences for the crust and mantle. *Chemical Geology*, *145*(3–4), 325–394. https://doi.org/10.1016/S0009-2541(97)00150-2

Putirka, K. D. (2008). Thermometers and barometers for volcanic systems. *Reviews in Mineralogy and Geochemistry*, *69*(1), 61–120. https://doi.org/10.2138/rmg.2008.69.3

Putirka, K. D., Perfit, M., Ryerson, F. J., & Jackson, M. G. (2007). Ambient and excess mantle temperatures, olivine thermometry, and active vs. passive upwelling. *Chemical Geology*, *241*(3–4), 177–206. https://doi.org/10.1016/j.chemgeo.2007.01.014

Qian, S.-P., Nichols, A. R. L., Zhang, L., Xu, Y.-G., Li, J., Guo, Y.-L., & Ren, Z.-Y. (2020). The mantle transition zone hosts the missing HIMU reservoir beneath Eastern China. *Geophysical Research Letters*, *47*(9), e2020GL087260. https://doi.org/10.1029/2020gl087260

Qian, S.-P., Zhou, H., Zhang, L., & Cheng, R. (2020). Mantle heterogeneity beneath the South China Sea: Chemical and isotopic evidence for contamination of ambient asthenospheric mantle. *Lithos*, *354–355*, 105335. https://doi.org/10.1016/j.lithos.2019.105335

Rizo, H., Andrault, D., Bennett, N. R., Humayun, M., Brandon, A., Vlastelic, I., et al. (2019). ^{182}W evidence for core-mantle interaction in the source of mantle plumes. *Geochemical Perspectives Letters*, *11*, 6–11. https://doi.org/10.7185/geochemlet.1917

Rudnick, R. L., & Gao, S. (2003). Composition of the continental crust. In R. L. Rudnick, H. D. Holland, & K. K. Turekian (Eds.), *Treatise on geochemistry* (pp. 1–64). Elsevier. https://doi.org/10.1016/B0-08-043751-6/03016-4

Sláma, J., Košler, J., Condon, D. J., Crowley, J. L., Gerdes, A., Hanchar, J. M., et al. (2008). Plešovice zircon—A new natural reference material for U–Pb and Hf isotopic microanalysis. *Chemical Geology*, *249*(1), 1–35. https://doi.org/10.1016/j.chemgeo.2007.11.005

Sleep, N. H. (1984). Tapping of magmas from ubiquitous mantle heterogeneities: An alternative to mantle plumes? *Journal of Geophysical Research*, *89*(B12), 10029–10041. https://doi.org/10.1029/JB089iB12p10029

Sobolev, A. V., Hofmann, A. W., Jochum, K. P., Kuzmin, D. V., & Stoll, B. (2011). A young source for the Hawaiian plume. *Nature*, *476*(7361), 434–437. https://doi.org/10.1038/nature10321

Sobolev, A. V., Hofmann, A. W., Kuzmin, D. V., Yaxley, G. M., Arndt, N. T., Chung, S. L., et al. (2007). The amount of recycled crust in sources of mantle-derived melts. *Science*, *316*(5823), 412–417. https://doi.org/10.1126/science.1138113

Soltanmohammadi, A., Grégoire, M., Rabinowicz, M., Gerbault, M., Ceuleneer, G., Rahgoshay, M., et al. (2018). Transport of volatile-rich melt from the mantle transition zone via compaction pockets: Implications for mantle metasomatism and the origin of alkaline lavas in the Turkish–Iranian Plateau. *Journal of Petrology*, *59*(12), 2273–2310. https://doi.org/10.1093/petrology/egy097

Stracke, A. (2012). Earth's heterogeneous mantle: A product of convection-driven interaction between crust and mantle. *Chemical Geology*, *330*, 274–299. https://doi.org/10.1016/j.chemgeo.2012.08.007

Stracke, A., Bizimis, M., & Salters, V. J. M. (2003). Recycling oceanic crust: Quantitative constraints. *Geochemistry, Geophysics, Geosystems*, *4*. https://doi.org/10.1029/2001gc000223

Sun, S. S., & Mcdonough, W. F. (1989). Chemical and isotopic systematics of oceanic basalts: Implications for mantle composition and processes. *Geological Society London Special Publications*, *42*(1), 313–345. https://doi.org/10.1144/GSL.SP.1989.042.01.19

Tanaka, T., Togashi, S., Kamioka, H., Amakawa, H., Kagami, H., Hamamoto, T., et al. (2000). JNdi-1: A neodymium isotopic reference in consistency with LaJolla neodymium. *Chemical Geology*, *168*(3), 279–281. https://doi.org/10.1016/S0009-2541(00)00198-4

Tatsumoto, M., Basu, A. R., Wankang, H., Junwen, W., & Guanghong, X. (1992). Sr, Nd, and Pb isotopes of ultramafic xenoliths in volcanic rocks of Eastern China: Enriched components EMI and EMII in subcontinental lithosphere. *Earth and Planetary Science Letters*, *113*(1), 107–128. https://doi.org/10.1016/0012-821X(92)90214-G

Thomson, A. R., Walter, M. J., Kohn, S. C., & Brooker, R. A. (2016). Slab melting as a barrier to deep carbon subduction. *Nature*, *529*(7584), 76–79. https://doi.org/10.1038/nature16174

Trela, J., Gazel, E., Sobolev, A. V., Moore, L., Bizimis, M., Jicha, B., & Batanova, V. G. (2017). The hottest lavas of the Phanerozoic and the survival of deep Archaean reservoirs. *Nature Geoscience*, *10*(6), 451–456. https://doi.org/10.1038/ngeo2954

Tschauner, O., Huang, S., Greenberg, E., Prakapenka, V. B., Ma, C., Rossman, G. R., et al. (2018). Ice-VII inclusions in diamonds: Evidence for aqueous fluid in Earth's deep mantle. *Science*, *359*(6380), 1136–1139. https://doi.org/10.1126/science.aao3030

Tu, K., Flower, M. F. J., Carlson, R. W., Xie, G., Chen, C.-Y., & Zhang, M. (1992). Magmatism in the South China Basin: 1. Isotopic and trace-element evidence for an endogenous Dupal mantle component. *Chemical Geology*, *97*(1), 47–63. https://doi.org/10.1016/0009-2541(92)90135-R

Wang, X. C., Li, Z. X., Li, X. H., Li, J., Liu, Y., Long, W. G., et al. (2012). Temperature, pressure, and composition of the mantle source region of late Cenozoic basalts in Hainan Island, SE Asia: A consequence of a young thermal mantle plume close to subduction zones? *Journal of Petrology*, *53*(1), 177–233. https://doi.org/10.1093/petrology/egr061

Wang, X. C., Li, Z. X., Li, X. H., Li, J., Xu, Y. G., & Li, X. H. (2013). Identification of an ancient mantle reservoir and young recycled materials in the source region of a young mantle plume: Implications for potential linkages between plume and plate tectonics. *Earth and Planetary Science Letters*, *377*, 248–259. https://doi.org/10.1016/j.epsl.2013.07.003

Wang, X.-J., Chen, L.-H., Hofmann, A. W., Mao, F.-G., Liu, J.-Q., Zhong, Y., et al. (2017). Mantle transition zone-derived EM1 component beneath NE China: Geochemical evidence from Cenozoic potassic basalts. *Earth and Planetary Science Letters*, *465*, 16–28. https://doi.org/10.1016/j.epsl.2017.02.028

Weiss, Y., Class, C., Goldstein, S. L., & Hanyu, T. (2016). Key new pieces of the HIMU puzzle from olivines and diamond inclusions. *Nature*, *537*, 666–670. https://doi.org/10.1038/nature19113

Wiedenbeck, M., Allé, P., Corfu, F., Griffin, W. L., Meier, M., Oberli, F., et al. (1995). Three natural zircon standards for U-Th-Pb, Lu-Hf, trace element and REE analyses. *Geostandards Newsletter*, *19*, 1–23. https://doi.org/10.1111/j.1751-908X.1995.tb00147.x

Willbold, M., & Stracke, A. (2010). Formation of enriched mantle components by recycling of upper and lower continental crust. *Chemical Geology*, *276*(3–4), 188–197. https://doi.org/10.1016/j.chemgeo.2010.06.005

Workman, R. K., Eiler, J. M., Hart, S. R., & Jackson, M. G. (2008). Oxygen isotopes in Samoan lavas: Confirmation of continent recycling. *Geology*, *36*(7), 551–554. https://doi.org/10.1130/g24558a.1

Workman, R. K., & Hart, S. R. (2005). Major and trace element composition of the depleted MORB mantle (DMM). *Earth and Planetary Science Letters*, *231*(1), 53–72. https://doi.org/10.1016/j.epsl.2004.12.005

Wu, H.-H., Tsai, Y.-B., Lee, T.-Y., Lo, C.-H., Hsieh, C.-H., & Toan, D. V. (2004). 3-D shear wave velocity structure of the crust and upper mantle in South China Sea and its surrounding regions by surface wave dispersion analysis. *Marine Geophysical Researches*, *25*(1), 5–27. https://doi.org/10.1007/s11001-005-0730-8

Xia, Q. K., Liu, J., Kovács, I., Hao, Y. T., Li, P., Yang, X. Z., et al. (2017). Water in the upper mantle and deep crust of eastern China: Concentration, distribution and implications. *National Science Review*, *6*, 125–144. https://doi.org/10.1093/nsr/nwx016

Xia, X.-P., Cui, Z.-X., Li, W., Zhang, W.-F., Yang, Q., Hui, H., & Lai, C.-K. (2019). Zircon water content: Reference material development and simultaneous measurement of oxygen isotopes by SIMS. *Journal of Analytical Atomic Spectrometry*, *34*(6), 1088–1097. https://doi.org/10.1039/C9JA00073A

Xu, X., O'Reilly, S. Y., Griffin, W. L., & Zhou, X. (2003). Enrichment of upper mantle peridotite: Petrological, trace element and isotopic evidence in xenoliths from SE China. *Chemical Geology*, *198*(3), 163–188. https://doi.org/10.1016/S0009-2541(03)00004-4

Yan, Q. S., Shi, X. F., Metcalfe, I., Liu, S., Xu, T., Kornkanitnan, N., et al. (2018). Hainan mantle plume produced late Cenozoic basaltic rocks in Thailand, Southeast Asia. *Scientific Reports*, *8*(1), 2640. https://doi.org/10.1038/s41598-018-20712-7

Yan, Q. S., Shi, X. F., Wang, K. S., Bu, W. R., & Xiao, L. (2008). Major element, trace element, and Sr, Nd and Pb isotope studies of Cenozoic basalts from the South China Sea. *Science in China Series D: Earth Sciences*, *51*(4), 550–566. https://doi.org/10.1007/s11430-008-0026-3

Yang, J., & Faccenda, M. (2020). Intraplate volcanism originating from upwelling hydrous mantle transition zone. *Nature*, *579*(7797), 88–91. https://doi.org/10.1038/s41586-020-2045-y

Yang, T., Liu, F., Harmon, N., Le, K. P., Gu, S., & Xue, M. (2015). Lithospheric structure beneath Indochina block from Rayleigh wave phase velocity tomography. *Geophysical Journal International*, *200*(3), 1582–1595. https://doi.org/10.1093/gji/ggu488

Yang, X. Z., Deloule, E., Xia, Q. K., Fan, Q. C., & Feng, M. (2008). Water contrast between Precambrian and Phanerozoic continental lower crust in eastern China. *Journal of Geophysical Research*, *113*, B08207. https://doi.org/10.1029/2007JB005541

Zhang, G.-L., Chen, L.-H., Jackson, M. G., & Hofmann, A. W. (2017). Evolution of carbonated melt to alkali basalt in the South China Sea. *Nature Geoscience*, *10*(3), 229–235. https://doi.org/10.1038/ngeo2877

Zhang, G.-L., Luo, Q., Zhao, J., Jackson, M. G., Guo, L.-S., & Zhong, L.-F. (2018). Geochemical nature of sub-ridge mantle and opening dynamics of the South China Sea. *Earth and Planetary Science Letters*, *489*, 145–155. https://doi.org/10.1016/j.epsl.2018.02.040

Zhang, L., Ren, Z.-Y., Xia, X.-P., Wang, C., & Qian, S.-P. (2018). An improved U-Pb age dating method for detrital zircon by LA-MC-ICP-MS. *Geochemical Journal*, *52*, 433–439. https://doi.org/10.2343/geochemj.2.0529

Zhang, L., Ren, Z.-Y., Xia, X.-P., Yang, Q., Hong, L.-B., & Wu, D. (2019). In situ determination of trace elements in melt inclusions using laser ablation inductively coupled plasma sector field mass spectrometry. *Rapid Communications in Mass Spectrometry*, *33*(4), 361–370. https://doi.org/10.1002/rcm.8359

Zhang, W.-F., Xia, X.-P., Eiichi, T., Li, L., Yang, Q., Zhang, Y.-Q., et al. (2020). Optimization of SIMS analytical parameters for water content measurement of olivine. *Surface and Interface Analysis*, *52*(5), 224–233. https://doi.org/10.1002/sia.6729

Zindler, A., & Hart, S. (1986). Chemical geodynamics. *Annual Review of Earth and Planetary Sciences*, *14*, 493–571. https://doi.org/10.1146/annurev.ea.14.050186.002425

Zou, H. B., & Fan, Q. C. (2010). U-Th isotopes in Hainan basalts: Implications for sub-asthenospheric origin of EM2 mantle endmember and the dynamics of melting beneath Hainan Island. *Lithos*, *116*(1–2), 145–152. https://doi.org/10.1016/j.lithos.2010.01.010

References From the Supporting Information

Danyushevsky, L. V., McNeill, A. W., & Sobolev, A. V. (2002). Experimental and petrological studies of melt inclusions in phenocrysts from mantle-derived magmas: An overview of techniques, advantages and complications. *Chemical Geology*, *183*(1–4), 5–24. https://doi.org/10.1016/S0009-2541(01)00369-2

Flower, M. F. J., Zhang, M., Chen, C.-Y., Tu, K., & Xie, G. (1992). Magmatism in the South China Basin: 2. Post-spreading Quaternary basalts from Hainan Island, south China. *Chemical Geology*, *97*(1), 65–87. https://doi.org/10.1016/0009-2541(92)90136-S

Fourny, A., Weis, D., & Scoates, J. S. (2016). Comprehensive Pb-Sr-Nd-Hf isotopic, trace element, and mineralogical characterization of mafic to ultramafic rock reference materials. *Geochemistry, Geophysics, Geosystems*, *17*(3), 739–773. https://doi.org/10.1002/2015GC006181

Govindaraju, G. (1994). Compilation of working values and sample description for 383 geostandards. *Geostandards Newsletter*, *18*, 1–158. https://doi.org/10.1111/j.1751-908x.1994.tb00526.x

Han, J. W., Xiong, X. L., & Zhu, Z. Y. (2009). Geochemistry of Late-Cenozoic basalts from Leiqiong area: The origin of EM2 and the contribution from sub-continental lithosphere mantle. *Acta Petrologica Sinica*, *25*(12), 3208–3220.

Hauri, E. H., & Hart, S. R. (1993). Re-Os isotope systematics of HIMU and EMII oceanic island basalts from the south Pacific Ocean. *Earth and Planetary Science Letters*, *114*, 353–371. https://doi.org/10.1016/0012-821X(93)90036-9

Hoàng, N., Flower, M. F. J., Chí, C. T., Xuân, P. T., Quý, H. V., & Sơn, T. T. (2013). Collision-induced basalt eruptions at Pleiku and Buôn Mê Thuột, south-central Viet Nam. *Journal of Geodynamics*, *69*, 65–83. https://doi.org/10.1016/j.jog.2012.03.012

Hu, S., Lin, Y., Zhang, J., Hao, J., Yang, W., & Deng, L. (2015). Measurements of water content and D/H ratio in apatite and silicate glasses using a NanoSIMS 50L. *Journal of Analytical Atomic Spectrometry*, *30*(4), 967–978. https://doi.org/10.1039/C4JA00417E

Jochum, K. P., Weis, U., Schwager, B., Stoll, B., Wilson, S. A., Haug, G. H., et al. (2016). Reference values following ISO guidelines for frequently requested rock reference materials. *Geostandards and Geoanalytical Research*, *40*(3), 333–350. https://doi.org/10.1111/j.1751-908X.2015.00392.x

Kamenetsky, V. S., Crawford, A. J., & Meffre, S. (2001). Factors controlling chemistry of magmatic spinel: An empirical study of associated olivine, Cr-spinel and melt inclusions from primitive rocks. *Journal of Petrology*, *42*(4), 655–671. https://doi.org/10.1093/petrology/42.4.655

Le Voyer, M., Kelley, K. A., Cottrell, E., & Hauri, E. H. (2017). Heterogeneity in mantle carbon content from CO_2-undersaturated basalts. *Nature Communications*, *8*(1), 14062. https://doi.org/10.1038/ncomms14062

Nishimura, K. (2012). A mathematical model of trace element and isotopic behavior during simultaneous assimilation and imperfect fractional crystallization. *Contributions to Mineralogy and Petrology*, *164*(3), 427–440. https://doi.org/10.1007/s00410-012-0745-5

Qian, S. P., Ren, Z. Y., Zhang, L., Hong, L. B., & Liu, J. Q. (2015). Chemical and Pb isotope composition of olivine-hosted melt inclusions from the Hannuoba basalts, North China Craton: Implications for petrogenesis and mantle source. *Chemical Geology*, *401*, 111–125. https://doi.org/10.1016/j.chemgeo.2015.02.018

Reisberg, L., Zindler, A., Marcantonio, F., White, W., Wyman, D., & Weaver, B. (1993). Os isotope systematics in ocean island basalts. *Earth and Planetary Science Letters*, *120*(3), 149–167. https://doi.org/10.1016/0012-821X(93)90236-3

Roeder, P. L., & Emslie, R. F. (1970). Olivine-liquid equilibrium. *Contributions to Mineralogy and Petrology*, *29*(4), 275–289. https://doi.org/10.1007/Bf00371276

Tu, K., Flower, M. F. J., Carlson, R. W., Zhang, M., & Xie, G. (1991). Sr, Nd, and Pb isotopic compositions of Hainan basalts (south China): Implications for a subcontinental lithosphere Dupal source. *Geology*, *19*(6), 567–569. https://doi.org/10.1130/0091-7613(1991)019<0567:snapic>2.3.co;2

Ulmer, P. (1989). The dependence of the Fe^{2+}-Mg cation-partitioning between olivine and basaltic liquid on pressure, temperature and composition. *Contributions to Mineralogy and Petrology*, *101*(3), 261–273. https://doi.org/10.1007/BF00375311

Widom, E., Horne, K. A., Shirey, S. B., & Schick, H.-U. (1999). Os isotope systematics in the Canary Islands and Madeira: Lithospheric contamination and mantle plume signatures. *Journal of Petrology*, *40*, 279–296. https://doi.org/10.1093/petroj/40.2.279

Yang, F., Huang, X.-L., Xu, Y.-G., & He, P.-L. (2019). Plume-ridge interaction in the South China Sea: Thermometric evidence from Hole U1431E of IODP Expedition 349. *Lithos*, *324–325*, 466–478. https://doi.org/10.1016/j.lithos.2018.11.031

Zhang, W., Xia, X., Zhang, Y., Peng, T., & Yang, Q. (2018). A novel sample preparation method for ultra-high vacuum (UHV) secondary ion mass spectrometry (SIMS) analysis. *Journal of Analytical Atomic Spectrometry*, *33*(9), 1559–1563. https://doi.org/10.1039/C8JA00087E

Zhou, P., & Mukasa, S. B. (1997). Nd-Sr-Pb isotopic, and major- and trace-element geochemistry of Cenozoic lavas from the Khorat Plateau, Thailand: Sources and petrogenesis. *Chemical Geology*, *137*(3), 175–193. https://doi.org/10.1016/S0009-2541(96)00162-3